ARTICLE

The actin homologue MreB organizes the bacterial cell membrane

Henrik Strahl[1], Frank Bürmann[2] & Leendert W. Hamoen[1,3]

The eukaryotic cortical actin cytoskeleton creates specific lipid domains, including lipid rafts, which determine the distribution of many membrane proteins. Here we show that the bacterial actin homologue MreB displays a comparable activity. MreB forms membrane-associated filaments that coordinate bacterial cell wall synthesis. We noticed that the MreB cytoskeleton influences fluorescent staining of the cytoplasmic membrane. Detailed analyses combining an array of mutants, using specific lipid staining techniques and spectroscopic methods, revealed that MreB filaments create specific membrane regions with increased fluidity (RIFs). Interference with these fluid lipid domains (RIFs) perturbs overall lipid homeostasis and affects membrane protein localization. The influence of MreB on membrane organization and fluidity may explain why the active movement of MreB stimulates membrane protein diffusion. These novel MreB activities add additional complexity to bacterial cell membrane organization and have implications for many membrane-associated processes.

[1] Centre for Bacterial Cell Biology, Institute for Cell and Molecular Biosciences, Newcastle University, Richardson Road, Newcastle NE2 4AX, UK. [2] Max Planck Institute of Biochemistry, Chromosome Organization and Dynamics, Am Klopferspitz 18, Martinsried D-82152, Germany. [3] Swammerdam Institute for Life Sciences (SILS), University of Amsterdam, Amsterdam 1098 XH, The Netherlands. Correspondence and requests for materials should be addressed to H.S. (email: h.strahl@ncl.ac.uk) or to L.W.H. (email: l.w.hamoen@uva.nl).

The morphology of many rod-shaped bacteria is established by the coordinated incorporation of new cell wall material perpendicular to the cell axis[1,2]. An essential component of this machinery is the bacterial actin homologue MreB, which polymerizes into filaments at the cell periphery[3]. The peripheral association of MreB is facilitated by a conserved hydrophobic membrane-binding loop, which in some organisms is further supported by a membrane-binding N-terminal amphipathic helix[4]. Upon binding, MreB forms a complex with the conserved membrane proteins MreC and MreD, and with proteins involved in peptidoglycan synthesis such as RodA, MurG, MraY, and several penicillin-binding proteins[1,2,5]. Interference with the MreB activity renders cells mechanically less rigid[6], and, in the absence of this, protein cells lose their rod-shaped morphology[7,8]. The prevailing model, in which helical MreB polymers spatially direct the synthesis of new peptidoglycan and as a result determine the general shape of the cell, has recently been revised. It turned out that MreB filaments, and the associated cell wall synthetic machinery, move around the cell in a process that is driven by peptidoglycan synthesis[9–11]. The MreB cytoskeleton has also been implicated in other cellular processes, including the establishment of cell polarity and chromosome segregation[12,13].

In a previous study, we have shown that the MreB cytoskeleton of *Bacillus subtilis* is sensitive to changes in the membrane potential, and incubation of cells with the proton ionophore CCCP results in a rapid delocalization of MreB[14]. The mechanism for this membrane potential sensitivity is currently unknown. During this work, we noticed that the fluorescence of the cell membrane, when stained with the lipid dye Nile Red, shows a rapid (within 1–2 min) transformation from a uniform to a clustered signal, which indicates irregularities in the lipid membrane. Interestingly, these Nile Red foci colocalize with GFP-MreB and do not emerge in bacteria that lack MreB. MreB is a homologue of eukaryotic actin, and actin forms an intricate membrane-associated network termed the cortical actin cytoskeleton[15]. The correlation between MreB and the lipid staining effects was intriguing since the cortical actin cytoskeleton is involved in the formation of lipid domains including lipid rafts and sphingolipid-enriched domains[15,16]. By applying different lipid staining techniques, and using a variety of mutant strains, we were able to show that the MreB cytoskeleton of *B. subtilis* is associated with fluid lipid domains, and, like the eukaryotic cortical actin cytoskeleton, is involved in the distribution of lipids and proteins. Furthermore, the active and directed movement of MreB appeared to stimulate the diffusion of proteins within the cell membrane. The consequences for membrane protein activity and cell wall synthesis are discussed.

Results

Altered membrane stain upon MreB delocalization. Dissipation of the membrane potential with CCCP results in delocalization of the cytoskeletal protein MreB in *B. subtilis*[14]. We noticed that such treatment also affects fluorescent membrane staining (Fig. 1a). In untreated cells, Nile Red stains cell membranes
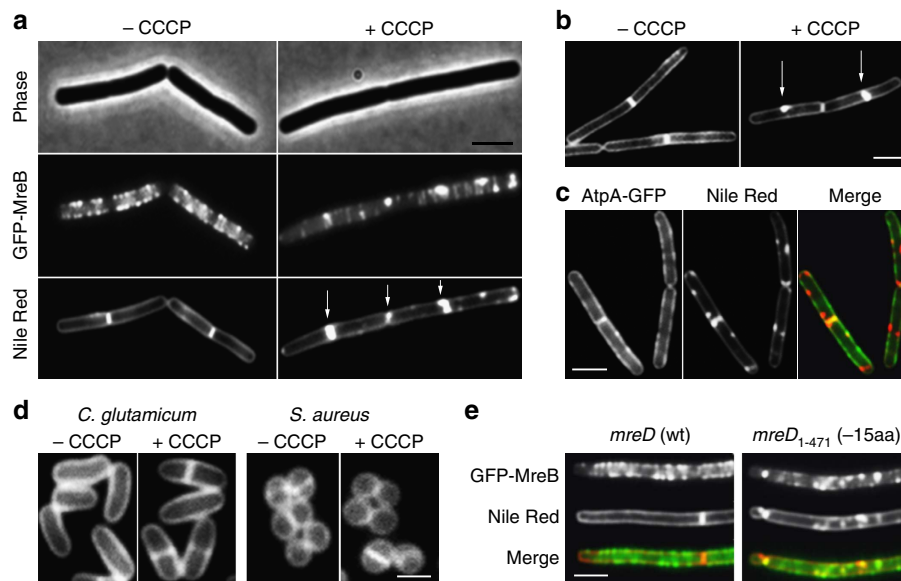
Figure 1 | Disruption of the MreB cytoskeleton is accompanied by an aberrant membrane stain. (a) Phase contrast images of *B. subtilis* cells (upper panel) expressing GFP-MreB (middle panel), and fluorescent Nile Red membrane stains (lower panel), are depicted in the absence or presence of the proton ionophore CCCP. Some of the Nile Red foci appearing with CCCP are highlighted with arrows (see Supplementary Fig. 5a for more examples). The CCCP-triggered local enrichment of MreB is not caused by the weak dimerization property of GFP, which was recently shown to stimulate protein clustering[69] (Supplementary Fig. 5b), or by artificial overproduction (Supplementary Fig. 6). Strain used: *B. subtilis* YK405 (*gfp-mreB*). **(b)** Incubation of F_1F_o ATP synthase-deficient cells with CCCP also results in a rapid (within 2 min) emergence of Nile Red foci, ruling out that the appearance of Nile Red foci is due to a reduction of ATP levels (see Supplementary Fig. 1c for more examples). Strain used: *B. subtilis* HS13 (Δ*atp*). **(c)** Comparison of Nile Red foci, and the localization of the integral membrane protein F_1F_o ATP synthase fused to GFP (AtpA-GFP). The lack of overlap in fluorescence signals rules out membrane invagination, or aberrantly formed septa (see arrows) as an explanation for the strong local Nile Red fluorescence (see Supplementary Fig. 4 for more examples). The reason that in some cases the Nile red stain appears to protrude into the cytoplasm is a consequence of high membrane fluorescence originating from slightly above and below the exact focal plane. Strain used: *B. subtilis* BS23 (*atpA-gfp*). **(d)** CCCP does not affect Nile Red fluorescent membrane stain in *Staphylococcus aureus* and *Corynebacterium glutamicum* which both lack MreB (see Supplementary Fig. 1d for more examples). Strains used: *C. glutamicum* RES167 and *S. aureus* RN4220. **(e)** Colocalization of GFP-MreB (upper panel) with Nile Red (middle panel) in *B. subtilis* strains encoding wild type MreD (wt), and a 15 amino acid C-terminal truncation of MreD (− 15aa), which results in a mild delocalization of MreB in low Mg^{2+} medium (see Supplementary Fig. 1e for more examples). Strains used *B. subtilis* HS35 (*gfp-mreB mreD* wt) and HS38 (*gfp-mreB mreD*$_{1-471}$/ − 15aa). Scale bar, 2 μm.

without a visible preference for certain membrane areas. A slightly stronger fluorescence signal is observed for division septa, which is caused by the presence of the two adjacent cell membranes from the newly formed daughter cells. However, in the presence of CCCP, brightly fluorescent foci appear. These membrane staining effects are visible within 2 min after CCCP addition. CCCP is a proton carrier that abolishes the proton motive force (pmf)-driven synthesis of ATP, resulting in a rapid reduction of the cellular ATP pool[14]. An F_1F_o ATP synthase deletion mutant is viable and generates ATP by pmf-independent means via glycolysis and is therefore able to maintain stable ATP levels when CCCP is present for a much longer period of time[14]. Nevertheless, in an F_1F_o ATP synthase deletion strain, the addition of CCCP still results in a spotty Nile Red membrane stain, indicating that the effect is not related to changes in ATP levels (Fig. 1b). Addition of the potassium-ionophore valinomycin also gives rise to an irregular fluorescence membrane staining, whereas the proton-potassium antiporter nigericin has no effect (Supplementary Fig. 1a). Valinomycin and nigericin dissipate the membrane potential and proton gradient, respectively. Therefore, the membrane staining effects specifically occur when the membrane potential is disturbed. The presence of chloramphenicol did not prevent these effects, indicating that *de novo* protein synthesis is not required (Supplementary Fig. 1b). The fact that the fluorescent foci become visible within 1 or 2 min makes it unlikely that they are formed by local accumulation of newly synthetized membrane material. A detailed analysis of the Nile Red fluorescence spectra showed that the increased Nile Red fluorescence originates from a regular lipid bilayer environment, and is not caused by Nile Red that is bound to abnormal protein or lipid aggregates (Supplementary Fig. 2). In theory, a loss of cell turgor as a result of CCCP treatment could result in the invagination of lipid membranes through plasmolysis. However, a dissipation of the membrane potential with CCCP does not cause a rapid loss of cell turgor (Supplementary Fig. 3). Moreover, when the Nile Red membrane stain was compared with the fluorescent membrane signal of a GFP-labelled transmembrane protein (F_1F_o ATP synthase), the GFP signal remained unaffected by CCCP and did not correlate with the fluorescent Nile Red foci (Fig. 1c; Supplementary Fig. 4). For these reasons, we conclude that the increase in fluorescence signal is not explained by invagination of the cell membrane, or otherwise abnormal membrane shapes.

Several experiments suggest a link between the CCCP-induced lipid staining effect and the MreB cytoskeleton. First, the Nile Red-stained membrane foci colocalize with clusters of MreB (Fig. 1a; Supplementary Fig. 5). Importantly, these clusters are not caused by artificial overproduction of a GFP-fusion protein (Supplementary Fig. 6). Second, both the irregular Nile Red stain and the delocalization of MreB are triggered by valinomycin and not by nigericin[14] (Supplementary Fig. 1a). Third, when the effect of CCCP on Nile Red staining was tested in *Staphylococcus aureus* or *Corynebacterium glutamicum*, which do not contain MreB homologues, no change in the fluorescent membrane stain was observed (Fig. 1d). Finally, the localization of *B. subtilis* MreB depends on MreD[17] and an MreD mutant that lacks the last 15 amino acids causes an irregular MreB pattern but also an uneven Nile Red stain (Fig. 1e). The latter experiment indicates that the membrane staining effect occurs upon delocalization of MreB, even when the membrane potential is not affected.

If the delocalization of MreB causes irregular fluorescent membrane signals, then the addition of CCCP should have no effect on the Nile Red membrane stain when MreB is absent. However, it appeared that CCCP still causes fluorescent Nile Red foci in the membrane of a *B. subtilis mreB* deletion mutant (Fig. 2a). *B. subtilis* encodes two other MreB homologues, Mbl

and MreBH, which are known to be able to complement the activity of MreB[7]. Individual deletions of *mbl* or *mreBH* do not prevent the formation of CCCP-induced Nile Red foci either, but in the absence of all three genes (ΔmreB, Δmbl, ΔmreBH) the Nile Red membrane stain showed a smooth fluorescence signal in the presence of CCCP (Fig. 2a, see Supplementary Fig. 7 for the analysis of the foci frequency). Importantly, the absence of Nile Red foci in the triple mutant is not a consequence of the deformation of the cell shape by the inhibition of lateral cell wall synthesis, since inactivation of RodA, which is required for peptidoglycan synthesis in the lateral cell wall[18], also results in round cells, yet these deformed cells still display Nile Red foci when CCCP is added (Fig. 2b). Taken together, these results support the suggestion that there is a correlation between MreB delocalization and the irregularities in Nile Red lipid stain.

Involvement of specific lipids. Cardiolipin (CL), phosphatidyl ethanolamine (PE) and phosphatidyl glycerol (PG) are the major phospholipid species in bacteria. Both CL and PE have been reported to form domains in *B. subtilis* membranes[19,20]. Nile Red is an uncharged fluorescent dye that partitions into lipid membranes based on its intrinsic hydrophobicity[21,22]. It is not known whether Nile Red prefers certain lipid head groups, but its fluorescence is sensitive to physical changes in its lipid environment[23]. To test whether an aberrant distribution of CL
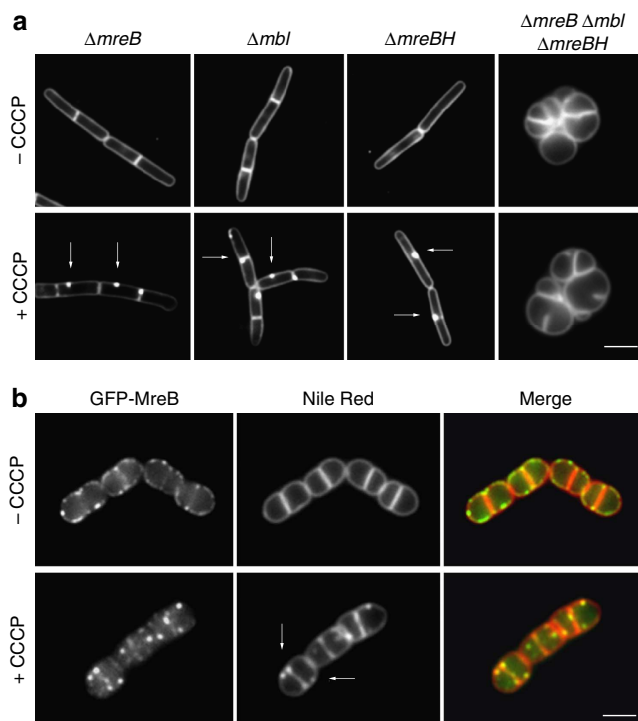
**Figure 2 | Distorted lipid staining requires the MreB cytoskeleton.**
(**a**) CCCP-dependent fluorescent Nile Red foci occur in *B. subtilis* strains deficient for single MreB homologues, but are absent in strains that lack all three MreB homologues (ΔmreB, Δmbl, ΔmreBH). Some of the Nile Red foci appearing with CCCP are highlighted with arrows. See also Supplementary Fig. 7 for the analysis of the foci frequency. Strains used: *B. subtilis* 3728 (ΔmreB), 4261 (Δmbl), 4262 (ΔmreBH) and 4277 (ΔmreB, Δmbl, ΔmreBH). (**b**) Colocalization of GFP-MreB (left panels) with Nile Red (middle panels) in *B. subtilis* cells depleted for RodA. The MreB cytoskeleton is disrupted with CCCP. Some of the Nile Red foci appearing with CCCP are highlighted with arrows. Strain used: *B. subtilis* HS36 (gfp-mreB Pspac-rodA). Scale bar, 2 μm.

or PE is responsible for the irregular Nile Red stain, CL- or PE-deficient *B. subtilis* mutant strains were treated with CCCP. Despite the absence of CL or PE in these strains[24], the fluorescent Nile Red foci still appear after depolarization of the membrane (Supplementary Fig. 8a).

Another commonly used membrane dye is FM 4-64, a styryl-dye that also partitions into lipid membrane surface based on intrinsic hydrophobicity[25]. Unlike Nile Red, it does carry a positive charge[25] and a preference to bind negatively charged lipid species can be speculated. It has been shown that this dye exhibits a fluorescent stain in *B. subtilis* cells that under certain conditions weakly resembles a MreB-like helical pattern[26,27]. This was interpreted as PG-enriched helical domains since PG is negatively charged, and these structures coalesce when PG is depleted[26,28]. However, it turned out that this change in an FM 4-64 staining pattern is caused by depolarization of the membrane potential upon PG depletion. As in case of uncharged Nile Red, addition of CCCP readily induced FM 4-64 foci that colocalize with MreB (see Supplementary Figs 8b–e and 9 for details). Thus, we conclude that FM 4-64 is not a specific indicator for PG. The strong formation of Nile Red foci upon depletion of PG makes it unlikely that these are specific clusters of PG. Together, these results suggest that the fluorescent membrane foci are not caused by domains enriched in lipids with specific head groups. A more probable explanation for the intense fluorescent Nile Red foci is the accumulation of lipids carrying specific fatty acid species.

Localization of fluid lipid domains. Bacterial membranes are composed of lipids that can form different conformations such as 'gel-phase' or a more fluid 'liquid-crystalline phase'. These distinct membrane configurations are predominantly determined by the fatty acid moiety of the lipids[29,30]. The presence of unsaturated bonds or branched chains increases the space that fatty acids occupy within a bilayer[31]. As a result, lipids containing unsaturated or branched fatty acids assemble into a more disordered 'liquid-crystalline phase', characterized by a less dense packing of lipids. In contrast, lipids with saturated fatty acids favour the more compact and less fluid 'gel-phase'. The fluidity of the membrane is known to influence the fluorescent staining of many lipid dyes, including that of Nile Red[23]. To test whether this is also the case in *B. subtilis* cells, we measured the fluorescence intensity of Nile Red using cells that differ in their membrane fluidity. In *B. subtilis* the fluid lipid content is greatly altered as a response to growth temperatures. To maintain a constant membrane fluidity at different temperatures, the fluid lipid content decreases with increasing growth temperature[32]. As a consequence, when cells grown at 48 °C are cooled down to 30 °C, their cell membrane will be less fluid compared with cells that are grown at 30 °C. As shown in Fig. 3a, this results in a lower Nile Red fluorescence intensity. In contrast, if cells are grown at room temperature, and subsequently transferred to 30 °C, the membrane fluidity is increased compared with cells grown at 30 °C. Indeed, this leads to an increase in Nile Red fluorescence (Fig. 3a). It is therefore possible that the irregular membrane stain caused by MreB delocalization points towards local differences in membrane fluidity.

To test whether the Nile Red foci are caused by the enrichment of fluid lipids, we adapted a staining technique used to visualize fluidity differences in eukaryotic membranes. The fluidity sensitive dye Laurdan undergoes an emission wavelength shift upon changes in fluidity that can be detected microscopically[33–36]. As shown in Fig. 3b and Supplementary Fig. 10, incubation with CCCP generates membrane areas with a clear and
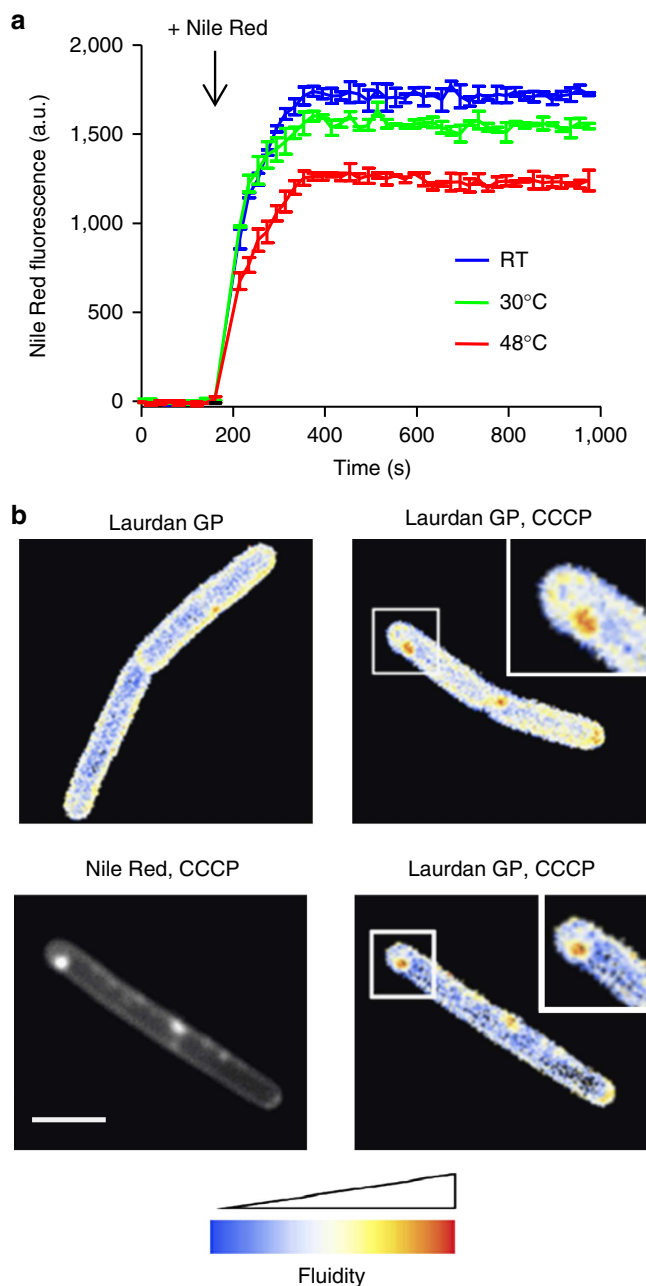
Figure 3 | Analysis of cell membrane fluidity. (**a**) Nile Red fluorescence intensity of *B. subtilis* cells grown in room temperature, 30 °C or 48 °C followed by shift to 30 °C, was measured fluorometrically. To prevent rapid adaptation of membrane fluidity[67], the measurements were carried out with a lipid desaturase (*des*)-deficient strain. The curves represent average values with s.d. of three replicate measurements. Strain used: *B. subtilis* HB5134 (Δ*des*). (**b**) Microscopic analysis of fluid membrane domains using Laurdan GP. The images show a colour-coded Laurdan GP intensity map in which red indicates regions of increased fluidity. Membrane fluidity is determined for untreated *B. subtilis* cells (left panel) and cells treated with CCCP (right panel). See also Supplementary Fig. 10 for the measurement of the average fluidity change. (**c**) Colocalization of Nile Red foci and Laurdan GP in CCCP-treated *B. subtilis* cells. Strain used: *B. subtilis* 168 (wild type). Scale bar, 2 μm.

statistically significant reduction in 'Laurdan Generalized Polarization', which indicates an increase in local membrane fluidity. Importantly, these membrane domains colocalize with Nile Red foci (Fig. 3c).

MreB generates membrane regions with increased fluidity. These experiments suggest a direct link between the MreB cytoskeleton and membrane regions with increased fluidity (RIFs). So far, we have only observed RIFs when MreB coalesces into large clusters, and the question arises whether RIFs are present under conditions in which MreB is normally localized, rather that delocalized by CCCP or other means. Presumably, visualization of RIFs in normal uninhibited cells requires a lipid dye with a high affinity for membrane areas with increased fluidity. It has been shown that a lipid-mimicking dye DiI-C12 localizes with high specificity to fluid membrane areas as a consequence of its relative short acyl chains[37,38]. When *B. subtilis* cells were stained with this dye, a distinct punctuated fluorescent pattern became visible that overlapped significantly with the GFP-MreB signal, with a Pearson's correlation coefficient of 0.9 (Fig. 4a–c; Supplementary Fig. 11a,b)[37]. As a control, we tested DiI-C18, a variant with longer acyl chains. Importantly, in this case, a smooth membrane stain is observed (Fig. 4a–c; Supplementary Fig. 11a,b), indicating that the fluorescent pattern of DiI-C12 is based on differences in membrane fluidity, and not a consequence of favoured interactions between the DiI head group and certain lipids or proteins.

The ability to visualize RIFs with DiI-C12 without dissipation of membrane potential allowed us to test which of the MreBCD proteins are required for RIF formation. In the absence of all three MreB homologues (ΔmreB, Δmbl, ΔmreBH), staining with DiI-C12 produces a smooth fluorescent membrane signal, and RIFs are no longer visible (Fig. 5a; Supplementary Fig. 11c). In contrast, *mreC* or *mreD* deletion strains that form comparably round cells still form RIFs (Fig. 5a; Supplementary Fig. 11c), indicating that the MreB homologues rather than the integral membrane proteins MreC or MreD are essential for RIF formation. MreB can bind directly to lipid bilayers[4], and, when GFP-MreB is expressed in a ΔmreBCD strain, a strong colocalization of GFP-MreB clusters with DiI-C12 foci is observed (Fig. 5b). These results show that the formation and spatial organization of RIFs is a specific property of MreB.

Absence of MreB changes membrane properties. Since MreB creates local membrane areas with increased fluidity, it might be that this activity affects the general fluidity of the cell membrane. Indeed, when the overall membrane fluidity was measured using Laurdan generalized polarization (GP), it turned out that the general membrane fluidity is significantly elevated when MreB homologues are absent (Fig. 6a). This increase in fluidity is comparable to the addition of 30 mM of the membrane fluidizer benzyl alcohol[39] (Fig. 6a). It should be added that growth in the absence of all three MreB homologues is only possible when the antisigma factor *rsgI* is deleted[40], however, a ΔrsgI mutation by itself does not result in altered membrane fluidity (Fig. 6a). ΔmreC or ΔmreD strains show identical changes in cell shape and inhibition of lateral cell wall synthesis as the triple *mreB mbl mreBH* deletion mutant but still contain RIF clusters. Importantly, the overall membrane fluidity of these strains is comparable to wild-type cells.

The Laurdan experiments suggest that RIFs formed by MreB affect the overall fluidity. However, it is possible that the absence of MreB influences the actual lipid composition. To investigate this, the fatty acid compositions of the different strains were analysed using gas chromatography (Fig. 6b; Supplementary Table 1). Both the ΔmreC mutant and *mreB* triple mutant (ΔmreB/mbl/mreBH) increase their overall fatty acid chain length (less C15 and more C17 species), which normally lowers the membrane fluidity (Fig. 6b; Supplementary Table 1). The ΔmreC, and to a lesser extent the *mreB* triple mutant, also increases the fraction of 'anteiso' fatty acids compared with 'iso' fatty acid species. Anteiso fatty acid species carry a methyl group attached to the third last carbon of the chain and are significantly more fluid than *iso* species, which carry a methyl group attached to the second last carbon[41]. In case of ΔmreC, this increase in anteiso fatty acids seems to compensate for the effect of increased fatty acid chain length since the overall membrane fluidity of this ΔmreC mutant is the same as for wild type (Fig. 6a). Importantly, this increase in anteiso fatty acids is lower in the *mreB* triple mutant compared with the ΔmreC mutant (Fig. 6b;
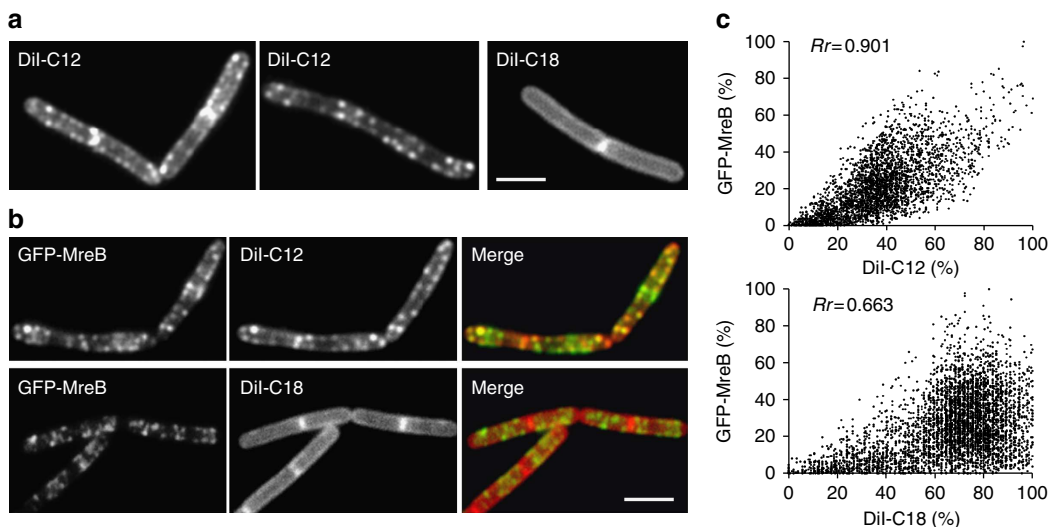
Figure 4 | Localization of RIFs in untreated *B. subtilis* cells. (**a**) RIFs can be visualized in normally growing untreated *B. subtilis* cells using the fluid membrane dye DiI-C12 (left panel). Staining with the long acyl-chain variant, DiI-C18, reveals a regular (smooth) membrane signal (right panel). Strain used: *B. subtilis* 168 (wild type). (**b**) Colocalization of DiI-C12 and GFP-MreB (see Supplementary Fig. 11 for more examples and statistical analysis of colocalization). Strain used: *B. subtilis* YK405 (*gfp-mreB*). (**c**) Fluorescence intensity correlation graphs are shown for the cells in panel **b**. The graphs display a pixel by pixel intensity correlation between DiI and GFP-MreB fluorescence, and shows the Pearson's correlation coefficients (*Rr*) (see Supplementary Fig. 11 for details). It should be mentioned that some fluorescence correlation between DiI-C18 and GFP remains since both DiI-C18 and MreB are present in the cell membrane. Strain used: *B. subtilis* YK405 (*gfp-mreB*). Scale bar, 2 μm.

Supplementary Table 1), and yet the overall fluidity of the MreB triple mutant is significantly higher (Fig. 6a). The strong increase of membrane fluidity of the *mreB* triple mutant can therefore not be explained by an altered fatty acid composition. This suggests that the MreB protein complex concentrates fluid lipids into RIFs, which results in lower overall membrane fluidity. These experiments provide further evidence for the specific role of MreB homologues in maintaining a proper lipid homeostasis in the cell membrane.
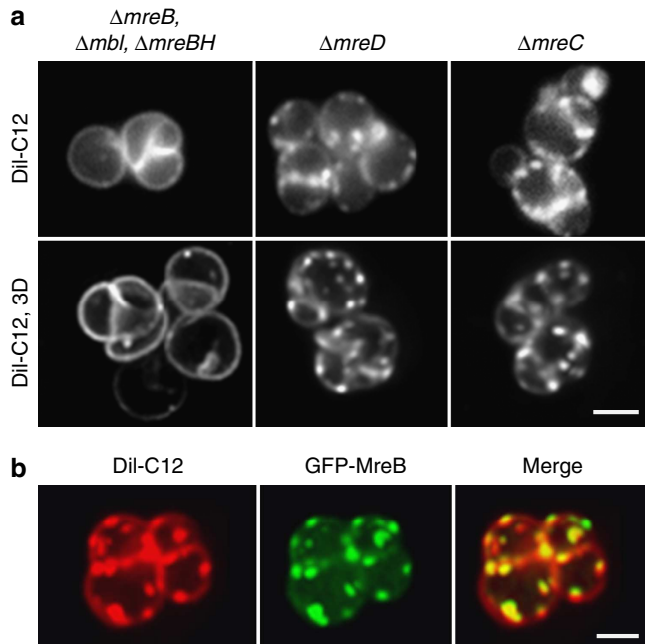

Figure 5 | DiI-C12-stained RIFs are MreB dependent. (a) DiI-C12 fluorescence of widefield (upper panel), and maximum intensity projection of a Z-stack (lower panel) of *B. subtilis* Δ*mreC* and Δ*mreD* cells, and cells that lack the three MreB homologues (Δ*mreB*, Δ*mbl*, Δ*mreBH*). See Supplementary Movie 1 for 3D-reconstruction, Supplementary Movie 2 for corresponding raw and deconvolved images, and Supplementary Fig. 11c for more examples. Strains used: *B. subtilis* 3481 (Δ*mreC*), 4311 (Δ*mreD*), 4277 (Δ*mreB*, Δ*mbl*, Δ*mreBH*, Δ*rsgI*). (b) Colocalization of DiI-C12 and GFP-MreB in the absence of MreBCD. The maximum intensity projections of Z-stacks are depicted. See Supplementary Movie 3 for 3D-reconstruction and Supplementary Movie 4 for corresponding raw and deconvolved images. Strain used: *B. subtilis* HS35 (*gfp-mreB* Δ*mreBCD*). Scale bar, 2 μm.

MreB is important for membrane protein distribution. The cortical actin cytoskeleton is involved in segregation of the eukaryotic cell membrane into domains that differ in fluidity, including the formation of lipid rafts[15,16,42–45]. This activity of actin influences the localization and diffusion of many membrane proteins[46–50]. Since MreB is an actin homologue and creates distinct membrane domains, the question arises whether the MreB cytoskeleton also influences the distribution of membrane proteins. To test this, the MreB cytoskeleton was disrupted with CCCP, and the localization of several integral membrane proteins was analysed. Indeed, incubation with CCCP induces clustering of several membrane proteins including Fructose permease (FruA), P16.7, YhaP and YqfD and RNase Y (Fig. 7a). Other proteins, such as succinate dehydrogenase (SdhA) and F_1F_o ATP synthase (AtpA), showed no apparent difference in localization pattern (Fig. 7a). The proteins FruA, YhaP, P16.7 and YqfD show a clear clustering with Nile Red foci in CCCP-treated cells (Supplementary Fig. 12). To test whether this clustering depends on MreB, and is not caused by CCCP itself, we analysed the localization of these proteins in the *mreB* triple mutant strain. Indeed, in this strain background, the localization of these proteins was unaffected by CCCP (Fig. 7b). Thus, the MreB-induced fluid lipid domains can influence the distribution of membrane proteins. It should be added that the localization pattern of RNase Y is still influenced by dissipation of membrane potential in *MreB* triple mutant (Fig. 7b), suggesting that in this case the effect is MreB independent.

MreB stimulates membrane protein diffusion. The MreB complexes of *B. subtilis* move rapidly along the cell membrane, driven by the cell wall synthesis machinery. This movement can be slowed down by inhibiting peptidoglycan synthesis with vancomycin[9,10]. Since MreB affects the localization of lipids and
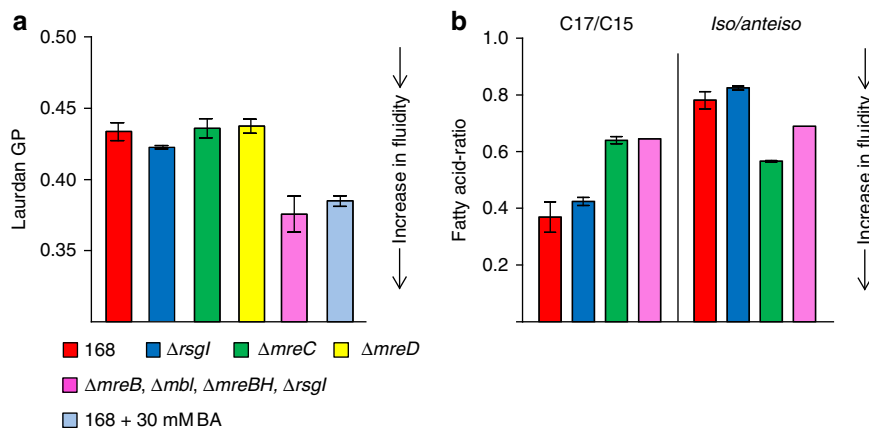
Figure 6 | Membrane fluidity increases in the absence of MreB. (a) Overall membrane fluidity of several cytoskeletal mutant strains was measured as Laurdan GP of logarithmically growing *B. subtilis* cells. As a positive control, an increase in fluidity (= decrease in Laurdan GP) was established by adding the membrane fluidizer benzyl alcohol (BA; 30 mM) to wild type cells. The diagram depicts the average values and s.d. of three independent measurements. (b) Ratios between chain lengths of the major fatty acids (C17 and C15) and ratios between the *iso* and *anteiso* forms of fatty acids are depicted for the different strains (see Supplementary Table 1 for the detailed composition). High C17/C15 or high *iso/anteiso* ratios indicate a reduced fluidity. The diagram depicts the average values and s.d. of two independent analyses. Strains used: *B. subtilis* 168 (wild type), 4264 (Δ*rsgI*), 3481 (Δ*mreC*), 4277 (Δ*mreB*, Δ*mbl*, Δ*mreBH*, Δ*rsgI*).
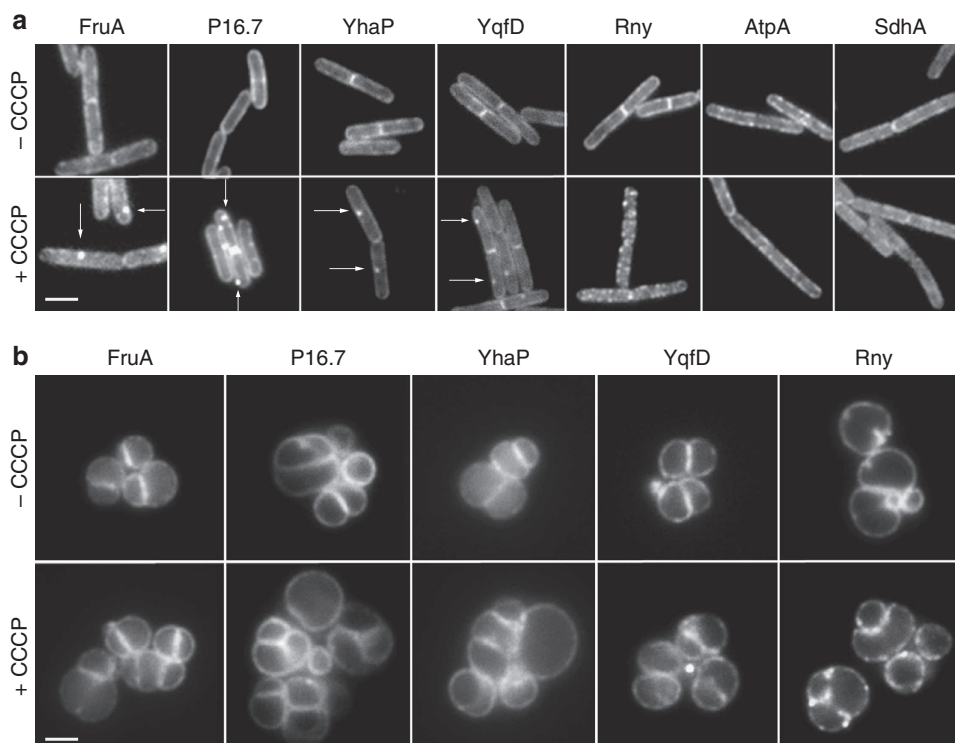
Figure 7 | Aberrant localization of different membrane proteins. (a) The localization of several membrane proteins (FruA, P16.7, YhaP, YqfD and Rny) is changed after the MreB cytoskeleton was disturbed by addition of CCCP. Some of the foci appearing with CCCP are highlighted with arrows. The localization of other proteins (AtpA and SdhA) remains unaffected. See Supplementary Fig. 12 for more examples, and colocalization with Nile Red. Strains used: *B. subtilis* FruA-GFP, 110WA (*p16.7-gfp*), *yhaP-gfp*, *yqfD-gfp*, 3569 (*rny-gfp*), BS23 (*atpA-gfp*), BS112 (*sdhA-gfp*). **(b)** The CCCP-induced clustering of membrane proteins FruA, P16.7, YhaP and YqfD is absent in strains deficient for MreB homologues. Strains used *B. subtilis* HS43 (*rny-gfp*, Δ*mreB**), HS44 (*fruA-gfp*, Δ*mreB**), HS45 (*P16.7-gfp*, Δ*mreB**), HS46 (*yhaP-gfp*, Δ*mreB**), HS47 (*yqfD-gfp*, Δ*mreB**). *mreB** designates (Δ*mreB*, Δ*mbl*, Δ*mreBH*, Δ*rsgI*). Scale bar, 2 μm.

membrane proteins, it is possible that the active movement of MreB also influences the diffusion dynamics of membrane proteins. To test this, the diffusion of several membrane proteins was followed using high-speed total internal reflection (TIRF) microscopy. As shown in the kymographs of Fig. 8a, the diffusion dynamics of FruA and F_1F_o ATP synthase changed significantly when the movement of MreB was stopped with vancomycin. The same behaviour was observed for two other tested transmembrane proteins (Supplementary Fig. 13a, see also Supplementary Fig. 13b for quantitation based on fluorescence intensity fluctuation).

In TIRF microscopy, a major determinant is the diffusion of GFP in and out of the range of the evanescent light. The reduction in membrane protein diffusion should thus increase photobleaching. Indeed, for all tested proteins, a significant increase in diffusion-limited GFP bleaching was observed in the presence of vancomycin (Fig. 8b,c; Supplementary Fig. 14). Thus, the active movement of the MreB cytoskeleton stimulates diffusion of membrane proteins.

Discussion

Despite their small size, the cell membrane of bacteria exhibits a remarkably complex organization. There are lipid species that accumulate at cell division sites and cell poles, and most membrane proteins are not uniformly distributed over the bacterial cell membrane[30,51,52]. In addition, it has been reported that *B. subtilis* can form low fluidity 'lipid rafts'[53–55]. The capacity of the MreB cytoskeleton to induce fluid lipid domains (RIFs)

that determine the distribution of membrane proteins adds a new dimension to this complexity.

The mechanism through which MreB organizes fluid lipids remains hypothetical. Peripheral membrane proteins have a capacity to induce lipid domains[56,57]. This activity is related to the binding of lipid bilayers by means of an intercalating amphipathic helix, but these domains are absent in MreB homologues from Gram-positive bacteria[4]. However, it has also been postulated that peripheral membrane proteins can directly induce fluid lipid domains by reducing the ordering effect of electrostatic attraction and repulsion between charged lipid head groups[58]. Although this mechanism is in good agreement with the electrostatic membrane-binding mode of MreB[4], we cannot rule out the involvement of other MreB-interacting proteins in the formation of RIFs.

Because of the various cellular functions of the cytoplasmic membrane, an organization into membrane areas that differ in their physical properties has a clear advantage. The optimal fluid state of the membrane is a compromise between different factors. On the one hand, high membrane fluidity promotes protein activity by reducing viscosity, and thus stimulating catalytic activity and diffusion of integral membrane proteins[59]. A higher membrane elasticity of fluid membranes also allows the lipid bilayer to optimally embed membrane proteins[60,61]. On the other hand, high membrane fluidity has the disadvantage that it increases proton permeability[32,62], resulting in a less efficient energy and ion homeostasis. The MreB-dependent formation of fluid lipid domains (RIFs) could therefore enable the cell to maintain an optimal condition for membrane protein activity in

limited areas of increased fluidity without compromising the proton permeability of the whole membrane.

In a recent study, it was shown that the random motion of chromosomes in bacterial and yeast cells is faster than that can be explained by simple Brownian motion. This increased molecular diffusion rate is caused by ATP-dependent processes such as RNA synthesis[63]. This bears some similarity with our observation that the diffusion of membrane proteins is also stimulated by an active process, in this case peptidoglycan synthesis, and the subsequent movement of RIFs. It is tempting to speculate that the continuous mixing of the cell membrane by active RIF movement promotes diffusion of proteins in a viscous membrane environment, thereby stimulating protein–protein and protein–substrate interactions.

Inactivation of MreB prevents lateral cell wall synthesis resulting in deformed round cells. This effect can be explained by the inability to recruit the necessary proteins to the proper site of synthesis. However, the fluid membrane environment created by MreB might also be required for optimal cell wall synthesis since Lipid II, the membrane-anchored precursor for peptidoglycan synthesis, has a strong preference for fluid membranes[64]. Possibly, RIFs are enriched with this essential precursor. In fact, the delocalization of MreB with CCCP does coincide with a loss of lateral Lipid II localization, based on staining with fluorescently-labelled vancomycin, whereas staining of the cell division septum remains unaffected (Supplementary Fig. 15).

With its ability to organize lipids and proteins in the bacterial cell membrane, MreB bears a functional resemblance to the eukaryotic cortical actin cytoskeleton[15,42,44,45]. There are, however, differences. The actin cytoskeleton forms a relatively static meshwork at the membrane periphery[65], yet the bacterial counterpart is more fragmented[9–11]. In eukaryotic cells, the membrane-anchored actin creates fences that restrict diffusion of proteins[65], whereas the active movement of the MreB cytoskeleton stimulates diffusion. Interestingly, it was recently shown that short and highly dynamic actin polymers, which influence clustering of membrane proteins, also exist in eukaryotic cells[48]. Thus, despite some differences, the ability of MreB and actin to induce and organize membrane domains appears comparable, and may explain why actin and MreB are evolutionarily linked.

Methods

Strains and growth conditions. The growth conditions and construction of strains are described in the Supplementary Materials and Methods. The used strains and conditions for gene induction are listed in Supplementary Table 2.

General fluorescence microscopy. For fluorescence microscopy, cells were grown to exponential growth phase at 30 °C if not stated otherwise. The cells were immobilized on microscope slides covered with a thin film of 1.2% agarose in water. For the dissipation of membrane potential with CCCP, the mounting medium was supplemented with 0.5% dimethylsulphoxide (DMSO) or 100 μM CCCP dissolved in DMSO (0.5% final concentration of DMSO). Imaging was carried out within 2 min after addition of ionophores. Membranes were visualized with Nile Red or FM 4-64 (0.5 μg ml^{-1}). Standard fluorescence microscopy was carried out using Zeiss Axiovert 200 M (Zeiss Plan-Neofluar × 100/1.30 Oil Ph3 objective), Nikon Eclipse Ti (Nikon Plan Fluor × 100/1.30 Oil Ph3 DLL objective),
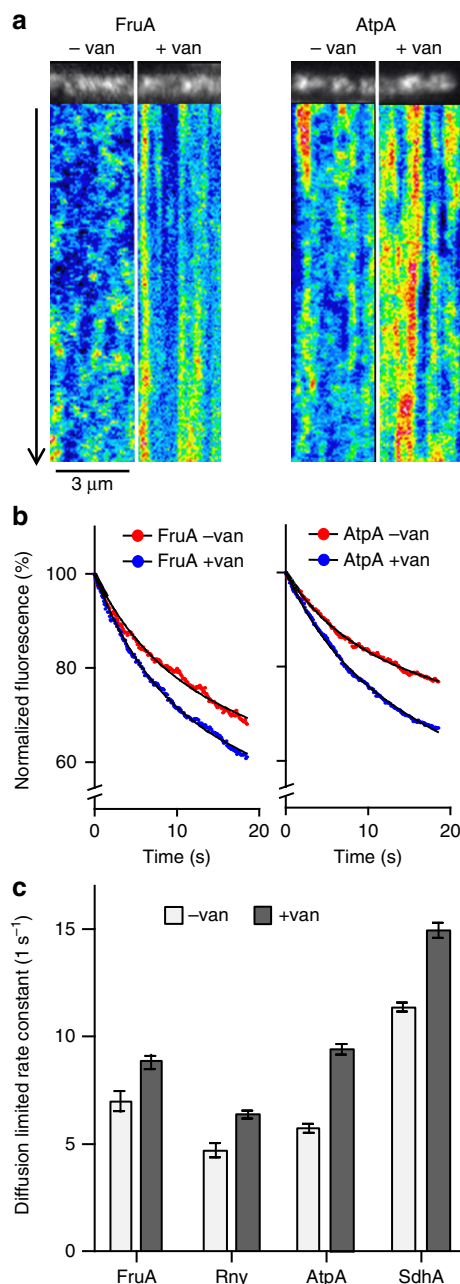
Figure 8 | MreB movement influences membrane protein diffusion. (**a**) Kymographs visualizing the diffusion of fructose permease (FruA) and F_1F_O ATP synthase (AtpA) in the absence and presence of vancomycin (van), which blocks MreB movement. Time lapse series with 20 s length and 100 ms time resolution was acquired using TIRF microscopy. See Supplementary Movie 5 for corresponding raw image series. (**b**) In TIRF microscopy, only proteins within the vicinity of the evanescent light (<200 nm distance from the coverslip surface) are subject to fluorophore (GFP) bleaching. The graphs depict the averaged, normalized and background-subtracted fluorescent signals of fructose permease (FruA) and F_1F_O ATP synthase (AtpA) in the presence (− van) and absence (+ van) of MreB movement. A significant increase in bleaching is observed when movement of MreB is inhibited with vancomycin, which indicates a reduced diffusion of proteins in and out of the range of the evanescent light. The curve fits were performed using a two-phase exponential decay model composed of a rapid bleaching of GFP within the range of the evanescent wave, and slower (diffusion limited) bleaching of the whole cell fluorescence (see Supplementary Fig. 14 for details). (**c**) Rate constants and s.e. of slow (diffusion limited) bleaching kinetics for Fructose permease (FruA), RNaseY (Rny), F_1F_O ATP synthase (AtpA) and Succinate dehydrogenase (SdhA) in the absence and presence of vancomycin. Increased rate constant indicates a reduced exchange of protein between the TIRF-illuminated area and rest of the cell surface. The number of analysed cells, goodness-of-fit and s.e. are provided in Supplementary Fig. 14. Strains used: *B. subtilis* BS23 (*atpA-gfp*), BS112 (*sdhA-gfp*), FruA-GFP and 3569 (*rny-gfp*).

and Applied Precision DeltaVision RT (Zeiss Plan-Neofluar 100x/1.30 Oil Ph3) microscopes. The images were acquired with Metamorph 6 (Molecular Devices), softWoRx Suite (Applied Precision), and further analysed using ImageJ v.1.38 (National Institutes of Health). Deconvolution was carried from optical sections using Huygens Essentials v.3.3 (Scientific Volume Imaging).

Laurdan GP microscopy. For the microscopic analysis of membrane fluidity, *B. subtilis* cells grown in LB medium were incubated for 5 min with 100 μM Laurdan, washed and then resuspended in fresh prewarmed LB. No inhibitory effect on growth was detected with 100 μM Laurdan. Laurdan was exited at 360 ± 20 nm, and fluorescence emission was captured at 528 ± 19 nm (exposure time: 500 ms) followed by a second image at 457 ± 25 nm (exposure time: 500 ms). Image analysis and generation of a colour-coded GP map were performed with Wolfram Mathematica 7 (Wolfram Research). In brief, the background fluorescence was subtracted, and GP values were calculated for each pixel, based on intensities values of the separate images, as $GP = (I_{457} - I_{528})/(I_{457} + I_{528})$, whereby I_{457} represents the emission intensity at 457 ± 25 nm and I_{528} emission intensity at 528 ± 19 nm. To remove signals not associated with cells, pixel pairs were regarded as insignificant when one of the channel intensities was below a threshold of 10% of the maximal values found in the membrane. Insignificant pixel pairs were assigned a GP of zero. Finally, GP pixel values were represented as a linear colour-coded GP map, whereby blue represents high GP values (low fluidity) and red represents low GP values (high fluidity). Insignificant pixels ($GP = 0$) are shown in black. The full Wolfram Mathematica-script can be obtained from the authors upon request. The ability of the microscope-based assay to detect changes in membrane fluidity was verified by measuring changes in membrane fluidity upon cold shock or incubation with 30 mM benzyl alcohol[66] (Supplementary Fig. 16a). For the measurement of mean GP values, the membrane fluorescence signal intensities at both emission channels were extracted as maximum values from a fluorescence intensity line scan perpendicular to the membrane plane. The values were measured for 70 individual cells, background subtracted, and the Laurdan GP values were calculated as described above. To prevent fast adaptation of membrane fluidity, a *B. subtilis* strain deficient for lipid desaturase (Δ*des*) was used in this case[67]. Des itself has no influence on the appearance of RIFs upon incubation with CCCP (Supplementary Fig. 16b).

Laurdan GP spectroscopy. For the measurement of membrane fluidity in batch cultures, cells were grown in LB supplemented with 0.1% glucose to an OD_{600} ∼0.5, followed by 5 min incubation with 10 μM Laurdan. Subsequently, cells were washed three times with prewarmed buffer containing 50 mM Na_2HPO_4/NaH_2PO_4 pH 7.4, 0.1% glucose and 150 mM NaCl with and without the membrane fluidizer benzyl alcohol (30 mM). In case of the different Mre-mutant strains, the media and buffers were supplemented with 20 mM $MgCl_2$. The Laurdan fluorescence intensities were measured at 435 ± 5 nm and 490 ± 5 nm upon excitation at 350 ± 10 nm, using a Tecan Infinite 200 M fluorometer. The Laurdan GP was calculated using the formula $GP = (I_{435} - I_{490})/(I_{435} + I_{490})$. In both microscopic and spectroscopic measurements, the Laurdan GP assay was able to reliably detect general changes in membrane fluidity, although, due to different excitation and emission wavelengths used, the absolute values obtained with microscopy slightly differed from the normal batch fluidity measurements (Supplementary Fig. 16a). The fluorescence emission spectrum of Laurdan was recorded using 10 μM Laurdan embedded in liposomes upon excitation with 350 nm light using a Tecan Infinite 200 M fluorometer. The liposomes were formed from *E. coli* polar lipids using detergent dialysis method. In brief, the lipid extract was solved in chloroform followed by evaporation under dry argon stream. The lipids were resolubilized in 25 mM Tris/HCl pH 7.4 and 1.5% octylglucoside (25 mg ml^{-1} lipids), followed by dialysis against 25 mM Tris/HCl pH 7.4. At last, the formed liposomes were diluted to 1:5 in H_2O and sized by extrusion through a 0.1-μm membrane.

DiI-C12 staining of fluid lipid domains. For staining of *B. subtilis* cells with DiI-C12, an overnight culture was diluted 1:100 in medium supplemented with 5 μg ml^{-1} DiI-C12 and 1% DMSO followed by growth for 2.5 h at 30 °C. Because of the high fluorescence of unbound dye, the stained cells were washed three times in prewarmed medium supplemented with 1% DMSO, followed by microscopy. The staining of *B. subtilis* with DiI-C18, which is insoluble in water, was carried out by suspending small amounts of solid DiI-C18 crystals in culture medium followed by 2.5 h incubation at 30 °C, based on a method described in Kim *et al.*[68] For microscopy, the crystals were removed by a brief low speed centrifugation. No growth inhibitory effect of the DiI-dyes was observed (Supplementary Fig. 17). For colocalization studies, the concentration of DiI-C12 was reduced to 2.5 μg ml^{-1}. The reason for this was the extensive overlap of the excitation spectra between DiI-C12 and GFP, which results in weak GFP fluorescence. The emission spectra of GFP and DiI-C12 are well separated, and no significant bleach-through of the emitted fluorescence was detected for DiI-C12 in the GFP channel, and *vice versa*.

TIRF time lapse microscopy. The analysis of membrane protein diffusion was carried out using a Nikon Eclipse Ti equipped with, Nikon CFI APO TIRF × 100/ 1.49 Oil objective, TIRF illumination module, Andor Xion X_3 EMCCD-camera and 488 nm solid state laser. The cells were imaged for 20 s with 100 ms time resolution

in a continuous illumination mode. The image analysis including the generation of kymographs was carried out using ImageJ v.1.38 (National Institutes of Health) and Multiple Kymograph plugin (J. Rietdorf and A. Seitz).

TIR-CP analysis. For the analysis of GFP-bleaching kinetics upon TIRF illumination, the average fluorescence intensity of cells was measured using an automated detection of cell area based on above background fluorescence intensity (ImageJ v.1.38, National Institutes of Health). In brief, the cell detection was performed using the first image frame and subsequently used to measure the average fluorescence intensity for each image of the time series. The background fluorescence signals were extracted from the same images as the average intensity of the remaining image area not associated with cells. The background subtracted and normalized intensity values were used to fit the GFP photobleach kinetics as mono- or biexponential decays using GraphPad Prism 5 (GraphPad Software). The fixation of GFP, applied to inhibit diffusion was performed by incubation of the cell samples with paraformaldehyde for 5 min at RT, followed by saturation of formaldehyde crosslinking by the addition of 100 mM Glycine.

Spectral imaging fluorescence microscopy. The analysis of the emission wavelength spectrum for Nile Red-stained *B. subtilis* cells was carried out with Nikon A1R point scanning confocal microscope using Nikon Plan Apo VC × 60 NA 1.4 oil objective and 561 nm excitation laser. The emission spectrum was recorded with a 4.8-nm window size for the total range of 570–749 nm. Image analysis was carried out with NIS-Elements 4.0 (Nikon).

Membrane fluidity-dependent Nile Red fluorescence intensity. Nile Red exhibits low fluorescence in a polar environment such as LB, but emits strongly when incorporated into hydrophobic cell membranes. This property was used to measure the intensity of Nile Red membrane fluorescence in *B. subtilis* cells grown in LB at different growth temperatures. For this, growing cultures were diluted to an optical density of $OD_{600} = 0.5$. Subsequently, the temperature of the cultures was rapidly adjusted to 30 °C, and the fluorescence increase was measured after addition of 0.5 μg ml^{-1} Nile Red. The measurements were carried out at 30 °C using a BMG Fluostar Optima fluorometer, and 584 nm excitation, and 620 nm emission filters. Background fluorescence was subtracted using signals measured from Nile Red in LB. To prevent rapid adaptation of membrane fluidity[67], the measurements were carried out with a lipid desaturase-deficient strain (*B. subtilis* Δ*des*).

Analysis of fatty acid composition. The fatty acid composition of *B. subtilis* wild-type cells and the cytoskeletal mutants was determined from cells grown at 30 °C in LB supplemented with 20 mM $MgCl_2$ that were collected when the cultures reached an OD_{600} of approximately 0.5. Fatty acids were analysed as fatty acid methyl esters using gas chromatography. All analyses were carried out in duplicates by the Identification Service of the DSMZ, Braunschweig, Germany.

References

1. Graumann, P. L. Cytoskeletal elements in bacteria. *Annu. Rev. Microbiol.* **61,** 589–618 (2007).
2. Margolin, W. Sculpting the bacterial cell. *Curr. Biol.* **19,** 812–822 (2009).
3. Eraso, J. M. & Margolin, W. Bacterial cell wall: thinking globally, actin locally. *Curr. Biol.* **21,** 628–630 (2011).
4. Salje, J., van den Ent, F., de Boer, P. & Lowe, J. Direct membrane binding by bacterial actin MreB. *Mol. Cell.* **43,** 478–487 (2011).
5. Mohammadi, T. *et al.* The essential peptidoglycan glycosyltransferase MurG forms a complex with proteins involved in lateral envelope growth as well as with proteins involved in cell division in *Escherichia coli*. *Mol. Microbiol.* **65,** 1106–1121 (2007).
6. Wang, S., Arellano-Santoyo, H., Combs, P. A. & Shaevitz, J. W. Actin-like cytoskeleton filaments contribute to cell mechanics in bacteria. *Proc. Natl Acad. Sci. USA* **107,** 9182–9185 (2010).
7. Formstone, A. & Errington, J. A magnesium-dependent *mreB* null mutant: implications for the role of *mreB*. in *Bacillus subtilis*. *Mol Microbiol.* **55,** 1646–1657 (2005).
8. Leaver, M. & Errington, J. Roles for MreC and MreD proteins in helical growth of the cylindrical cell wall in *Bacillus subtilis*. *Mol. Microbiol.* **57,** 1196–1209 (2005).
9. Dominguez-Escobar, J. *et al.* Processive movement of MreB-associated cell wall biosynthetic complexes in bacteria. *Science* **333,** 225–228 (2011).
10. Garner, E. C. *et al.* Coupled, circumferential motions of the cell wall synthesis machinery and MreB filaments in *B. subtilis*. *Science* **333,** 222–225 (2011).
11. van Teeffelen, S. *et al.* The bacterial actin MreB rotates, and rotation depends on cell-wall assembly. *Proc. Natl Acad. Sci. USA* **108,** 15822–15827 (2011).
12. Shaevitz, J. W. & Gitai, Z. The structure and function of bacterial actin homologs. *Cold Spring Harb. Perspect. Biol.* **2,** a000364 (2010).
13. Carballido-Lopez, R. The bacterial actin-like cytoskeleton. *Microbiol. Mol. Biol. Rev.* **70,** 888–909 (2006).

14. Strahl, H. & Hamoen, L. W. Membrane potential is important for bacterial cell division. *Proc. Natl Acad. Sci. USA* **107,** 12281–12286 (2010).

15. Chichili, G. R. & Rodgers, W. Cytoskeleton-membrane interactions in membrane raft structure. *Cell. Mol. Life Sci.* **66,** 2319–2328 (2009).

16. Frisz, J. F. *et al.* Direct chemical evidence for sphingolipid domains in the plasma membranes of fibroblasts. *Proc. Natl Acad. Sci. USA* **110,** E613–E622 (2013).

17. Defeu, S. H. J. & Graumann, P. L. *Bacillus subtilis* actin-like protein MreB influences the positioning of the replication machinery and requires membrane proteins MreC/D and other actin-like proteins for proper localization. *BMC Cell Biol.* **6,** 10 (2005).

18. de Pedro, M. A., Donachie, W. D., Holtje, J. V. & Schwarz, H. Constitutive septal murein synthesis in *Escherichia coli* with impaired activity of the morphogenetic proteins RodA and penicillin-binding protein 2. *J. Bacteriol.* **183,** 4115–4126 (2001).

19. Mileykovskaya, E. & Dowhan, W. Cardiolipin membrane domains in prokaryotes and eukaryotes. *Biochim. Biophys. Acta* **1788,** 2084–2091 (2009).

20. Matsumoto, K., Kusaka, J., Nishibori, A. & Hara, H. Lipid domains in bacterial membranes. *Mol. Microbiol.* **61,** 1110–1117 (2006).

21. Mukherjee, S., Raghuraman, H. & Chattopadhyay, A. Membrane localization and dynamics of Nile Red: effect of cholesterol. *Biochim. Biophys. Acta* **1768,** 59–66 (2007).

22. Greenspan, P. & Fowler, S. D. Spectrofluorometric studies of the lipid probe, nile red. *J. Lipid Res.* **26,** 781–789 (1985).

23. Kucherak, O. A. *et al.* Switchable nile red-based probe for cholesterol and lipid order at the outer leaflet of biomembranes. *J. Am. Chem. Soc.* **132,** 4907–4916 (2010).

24. Salzberg, L. I. & Helmann, J. D. Phenotypic and transcriptomic characterization of *Bacillus subtilis* mutants with grossly altered membrane composition. *J. Bacteriol.* **190,** 7797–7807 (2008).

25. Wu, Y., Yeh, F. L., Mao, F. & Chapman, E. R. Biophysical characterization of styryl dye-membrane interactions. *Biophys. J.* **97,** 101–109 (2009).

26. Barak, I., Muchova, K., Wilkinson, A. J., O'Toole, P. J. & Pavlendova, N. Lipid spirals in *Bacillus subtilis* and their role in cell division. *Mol. Microbiol.* **68,** 1315–1327 (2008).

27. Muchova, K., Wilkinson, A. J. & Barak, I. Changes of lipid domains in *Bacillus subtilis* cells with disrupted cell wall peptidoglycan. *FEMS Microbiol. Lett.* **325,** 92–98 (2011).

28. Hashimoto, M. *et al.* Induction of extracytoplasmic function sigma factors in *Bacillus subtilis* cells with membranes of reduced phosphatidylglycerol content. *Genes. Genet. Syst.* **84,** 191–198 (2009).

29. Zhang, Y. M. & Rock, C. O. Membrane lipid homeostasis in bacteria. *Nat. Rev. Microbiol.* **6,** 222–233 (2008).

30. Vanounou, S., Pines, D., Pines, E., Parola, A. H. & Fishov, I. Coexistence of domains with distinct order and polarity in fluid bacterial membranes. *Photochem. Photobiol.* **76,** 1–11 (2002).

31. Hazel, J. R. & Williams, E. E. The role of alterations in membrane lipid composition in enabling physiological adaptation of organisms to their physical environment. *Prog. Lipid Res.* **29,** 167–227 (1990).

32. van de Vossenberg, J. L. C. M., Driessen, A. J. M., da Costa, M. S. & Konings, W. N. Homeostasis of the membrane proton permeability in *Bacillus subtilis* grown at different temperatures. *Biochim. Biophys. Acta.* **1419,** 97–104 (1999).

33. Parasassi, T., De Stasio, G., d'Ubaldo, A. & Gratton, E. Phase fluctuation in phospholipid membranes revealed by Laurdan fluorescence. *Biophys. J.* **57,** 1179–1186 (1990).

34. Tyler, K. M. & Wheeler, G. Widefield microscopy for live imaging of lipid domains and membrane dynamics. *Biochim. Biophys. Acta* **1808,** 634–641 (2011).

35. Mercier, R., Domínguez-Cuevas, P. & Errington, J. Crucial role for membrane tluidity in proliferation of primitive cells. *Cell Rep.* **1,** 417–423 (2012).

36. Bach, J. N. & Bramkamp, M. Flotillins functionally organize the bacterial membrane. *Mol. Microbiol.* **88,** 1205–1217 (2013).

37. Baumgart, T., Hunt, G., Farkas, E. R., Webb, W. W. & Feigenson, G. W. Fluorescence probe partitioning between Lo/Ld phases in lipid membranes. *Biochim. Biophys. Acta* **1768,** 2182–2194 (2007).

38. Zhao, J., Wu, J. & Veatch, Sarah L. Adhesion stabilizes robust lipid heterogeneity in supercritical membranes at physiological temperature. *Biophys. J.* **104,** 825–834 (2013).

39. Konopásek, I., Strzalka, K. & Svobodová, J. Cold shock in *Bacillus subtilis*: different effects of benzyl alcohol and ethanol on the membrane organisation and cell adaptation. *Biochim. Biophys. Acta* **1464,** 18–26 (2000).

40. Schirner, K. & Errington, J. The cell wall regulator σI specifically suppresses the lethal phenotype of *mbl* mutants in *Bacillus subtilis*. *J. Bacteriol.* **191,** 1404–1413 (2009).

41. de Mendoza, D., Schujman, G. S. & Aguilar, P. S. Biosynthesis and function of membrane lipids. in *Bacillus subtilis And Its Relatives: From Genes To Cells.* (eds Sonenshein, A. L., Hoch, J. A. & Losick, R.) 43–55 (ASM Press, 2001).

42. Liu, A. P. & Fletcher, D. A. Actin polymerization serves as a membrane domain switch in model lipid bilayers. *Biophys. J.* **91,** 4064–4070 (2006).

43. McMahon, H. T. & Gallop, J. L. Membrane curvature and mechanisms of dynamic cell membrane remodelling. *Nature* **438,** 590–596 (2005).

44. Petrov, E. P., Ehrig, J. & Schwille, P. Near-critical fluctuations and cytoskeleton-assisted phase separation lead to subdiffusion in cell membranes. *Biophys. J.* **100,** 80–89 (2011).

45. Veatch, S. L., Machta, B. B., Papanikolaou, S. & Sethna, J. P. Minimal model of plasma membrane heterogeneity requires coupling cortical actin to criticality. *Biophys. J.* **100,** 1668–1677 (2011).

46. Lucero, H. A. & Robbins, P. W. Lipid rafts-protein association and the regulation of protein activity. *Arch. Biochem. Biophys.* **426,** 208–224 (2004).

47. Derivery, E., Helfer, E., Henriot, V. & Gautreau, A. Actin polymerization controls the organization of WASH domains at the surface of endosomes. *PLoS One* **7,** e39774 (2012).

48. Gowrishankar, K. *et al.* Active remodeling of cortical actin regulates spatio-temporal organization of cell surface molecules. *Cell* **149,** 1353–1367 (2012).

49. Gomez-Llobregat, J., Buceta, J. & Reigada, R. Interplay of cytoskeletal activity and lipid phase stability in dynamic protein recruitment and clustering. *Sci. Rep.* **3,** 2608 (2013).

50. Lavi, Y., Gov, N., Edidin, M. & Gheber, L. A. Lifetime of major histocompatibility complex class-I membrane clusters is controlled by the actin cytoskeleton. *Biophys. J.* **102,** 1543–1550 (2012).

51. Vanounou, S., Parola, A. H. & Fishov, I. Phosphatidylethanolamine and phosphatidylglycerol are segregated into different domains in bacterial membrane. Study with pyrene-labeled phospholipids. *Biophys. J.* **82,** 343a–343a (2002).

52. Johnson, A. S., van Horck, S. & Lewis, P. J. Dynamic localization of membrane proteins in *Bacillus subtilis*. *Microbiology* **150,** 2815–2824 (2004).

53. Lopez, D. & Kolter, R. Functional microdomains in bacterial membranes. *Genes Dev.* **24,** 1893–1902 (2010).

54. Donovan, C. & Bramkamp, M. Characterization and subcellular localization of a bacterial flotillin homologue. *Microbiology* **155,** 1786–1799 (2009).

55. Dempwolff, F., Moller, H. M. & Graumann, P. L. Synthetic motility and cell shape defects associated with deletions of flotillin/reggie paralogs in *Bacillus subtilis* and interplay of these proteins with NfeD proteins. *J. Bacteriol.* **194,** 4652–4661 (2012).

56. Garcia-Saez, A. J., Chiantia, S. & Schwille, P. Effect of line tension on the lateral organization of lipid membranes. *J. Biol. Chem.* **282,** 33537–33544 (2007).

57. Cornell, R. B. & Taneva, S. G. Amphipathic helices as mediators of the membrane interaction of amphitropic proteins, and as modulators of bilayer physical properties. *Curr. Protein Pept. Sci.* **7,** 539–552 (2006).

58. Mbamala, E. C., Ben-Shaul, A. & May, S. Domain formation induced by the adsorption of charged proteins on mixed lipid membranes. *Biophys. J.* **88,** 1702–1714 (2005).

59. Lee, A. G. How lipids affect the activities of integral membrane proteins. *Biochim. Biophys. Acta* **1666,** 62–87 (2004).

60. Andersen, O. S. & Koeppe, R. E. Bilayer thickness and membrane protein function: An energetic perspective. *Annu. Rev. Bioph. Biom.* **36,** 107–130 (2007).

61. Cybulski, L. E. & de Mendoza, D. Bilayer hydrophobic thickness and integral membrane protein function. *Curr. Protein Pept Sci.* **12,** 760–766 (2011).

62. Rossignol, M., Thomas, P. & Grignon, C. Proton permeability of liposomes from natural phospholipid mixtures. *Biochim. Biophys. Acta* **684,** 195–199 (1982).

63. Weber, S. C., Spakowitz, A. J. & Theriot, J. A. Nonthermal ATP-dependent fluctuations contribute to the *in vivo* motion of chromosomal loci. *Proc. Natl Acad. Sci. USA* **109,** 7338–7343 (2012).

64. Ganchev, D. N., Hasper, H. E., Breukink, E. & de Kruijff, B. Size and orientation of the lipid II headgroup as revealed by AFM imaging. *Biochemistry* **45,** 6195–6202 (2006).

65. Kusumi, A. *et al.* Paradigm shift of the plasma membrane concept from the two-dimensional continuum fluid to the partitioned fluid: high-speed single-molecule tracking of membrane molecules. *Annu. Rev. Bioph. Biom.* **34,** 351–354 (2005).

66. Konopasek, I., Strzalka, K. & Svobodova, J. Cold shock in *Bacillus subtilis*: different effects of benzyl alcohol and ethanol on the membrane organisation and cell adaptation. *Biochim. Biophys. Acta* **1464,** 18–26 (2000).

67. Weber, M. H., Klein, W., Muller, L., Niess, U. M. & Marahiel, M. A. Role of the *Bacillus subtilis* fatty acid desaturase in membrane adaptation during cold shock. *Mol. Microbiol.* **39,** 1321–1329 (2001).

68. Kim, B. G., Dai, H. N., McAtee, M., Vicini, S. & Bregman, B. S. Labeling of dendritic spines with the carbocyanine dye DiI for confocal microscopic imaging in lightly fixed cortical slices. *J. Neurosci. Methods* **162,** 237–243 (2007).

69. Landgraf, D., Okumus, B., Chien, P., Baker, T. A. & Paulsson, J. Segregation of molecules at cell division reveals native protein localization. *Nat. Methods* **9,** 480–498 (2012).

Author contributions

H.S and F.B. carried out the experiments; H.S. and L.W.H. designed the project, analysed the data and wrote the paper.

Additional information

Supplementary Information accompanies this paper at http://www.nature.com/naturecommunications

Competing financial interests: The authors declare no competing financial interests.

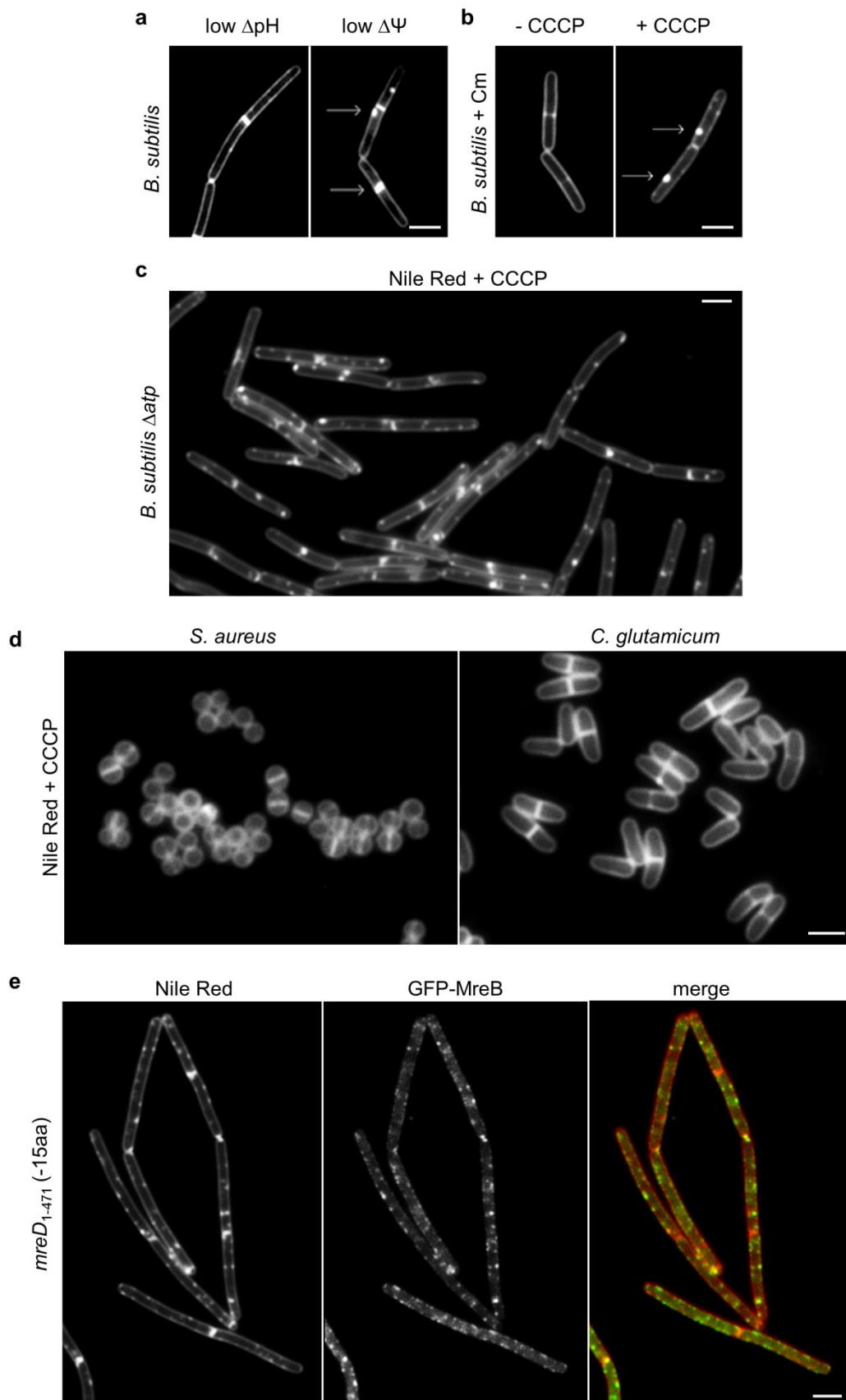**Reprints and permission** information is available online at http://npg.nature.com/reprintsandpermissions/

How to cite this article: Strahl, H. *et al.* The actin homologue MreB organizes the bacterial cell membrane. *Nat. Commun.* 5:3442 doi: 10.1038/ncomms4442 (2014).

SUPPLEMENTARY FIGURES

Supplementary Figure 1

CCCP induced changes in Nile Red stain are caused by delocalization of MreB

(a) CCCP is a specific proton-ionophore that dissipates the proton motive force (pmf), composed of the membrane potential ($\Delta\Psi$) and the transmembrane pH gradient (ΔpH). To determine which of these factors is responsible for the irregular Nile Red stain, the membrane potential was dissipated with the K^+ ionophore valinomycin ('low $\Delta\Psi$'), and the transmembrane pH gradient by the H^+/K^+ antiporter nigericin ('low ΔpH') [1]. Only dissipation of the $\Delta\Psi$ triggers the emergence of Nile Red foci (left panels). Some of the Nile Red foci are highlighted with arrows. Strain used: *B. subtilis* 168 wild type. (b) Inhibition of protein synthesis by 5 min pre-incubation with 100 µg/ml chloramphenicol does not prevent CCCP-induced Nile Red foci, indicating that *de novo* protein synthesis is not required. Some of the Nile Red foci are highlighted with arrows. Strain used: *B. subtilis* 168 wild type. (c) Incubation of F_1F_o ATP-synthase deficient cells with CCCP still results in a rapid emergence of Nile Red foci. This is a larger field of cells shown in Figure 1b. Strain used: *B. subtilis* HS13 (Δatp). (d) CCCP does not affect Nile Red fluorescent membrane stain in *Staphylococcus aureus* and *Corynebacterium glutamicum*. This is a larger field of cells shown in Figure 1d. Strains used: *C. glutamicum* RES167, and *S. aureus* RN4220. (e) Colocalization of GFP-MreB with Nile Red foci (middle panel) in *B. subtilis* strain encoding a 15 amino acid C-terminal truncation of MreD (-15aa) that results in a mild delocalization of MreB. This is a larger field of cells shown in Figure 1e. Strain used: *B. subtilis* HS38 *(gfp-mreB mreD1-471/-15aa)*. Scale bar, 2 µm.

Supplementary Figure 2
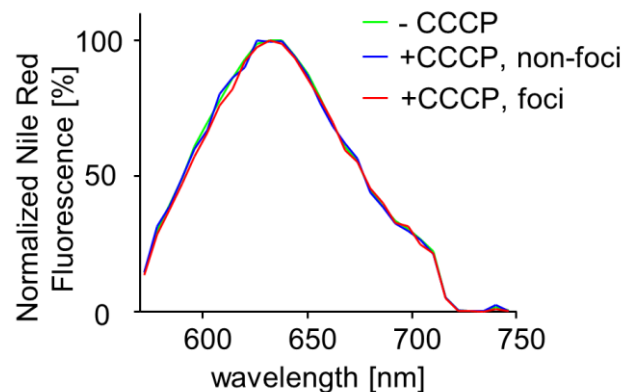
CCCP-induced Nile Red-foci have a regular lipid bilayer structure

The emission spectrum of Nile Red is highly sensitive to its environment and exhibits specific spectral shifts that are commonly used to detect and identify changes in lipid aggregation, and which is used to distinguish the protein and membrane embedded states [2, 3, 4]. To test whether the CCCP-induced Nile Red foci are characterized by binding to protein aggregates, or non-bilayer lipid aggregates, the emission spectrum of Nile red was recorded using spectral imaging fluorescence microscopy. This microscopic technique allows recording of fluorescent wavelength spectra with spatial resolution. The average and normalized spectra of 10 individual CCCP-induced foci are compared against spectra obtained from non-foci areas of CCCP treated cells, and from untreated cells (see Materials and Methods). In all cases, the emission spectra are essentially indistinguishable, indicating that the fluorophore still emits from a regular lipid bilayer environment in the Nile Red foci, and the increased fluorescence is not caused by staining of possible aggregated proteins or lipids. Strain used: *B. subtilis* 168 (wild type).

Supplementary Figure 3

a

b

c

d

Nile Red   Nile Red + CCCP   Nile Red + CCCP (hypotonic)
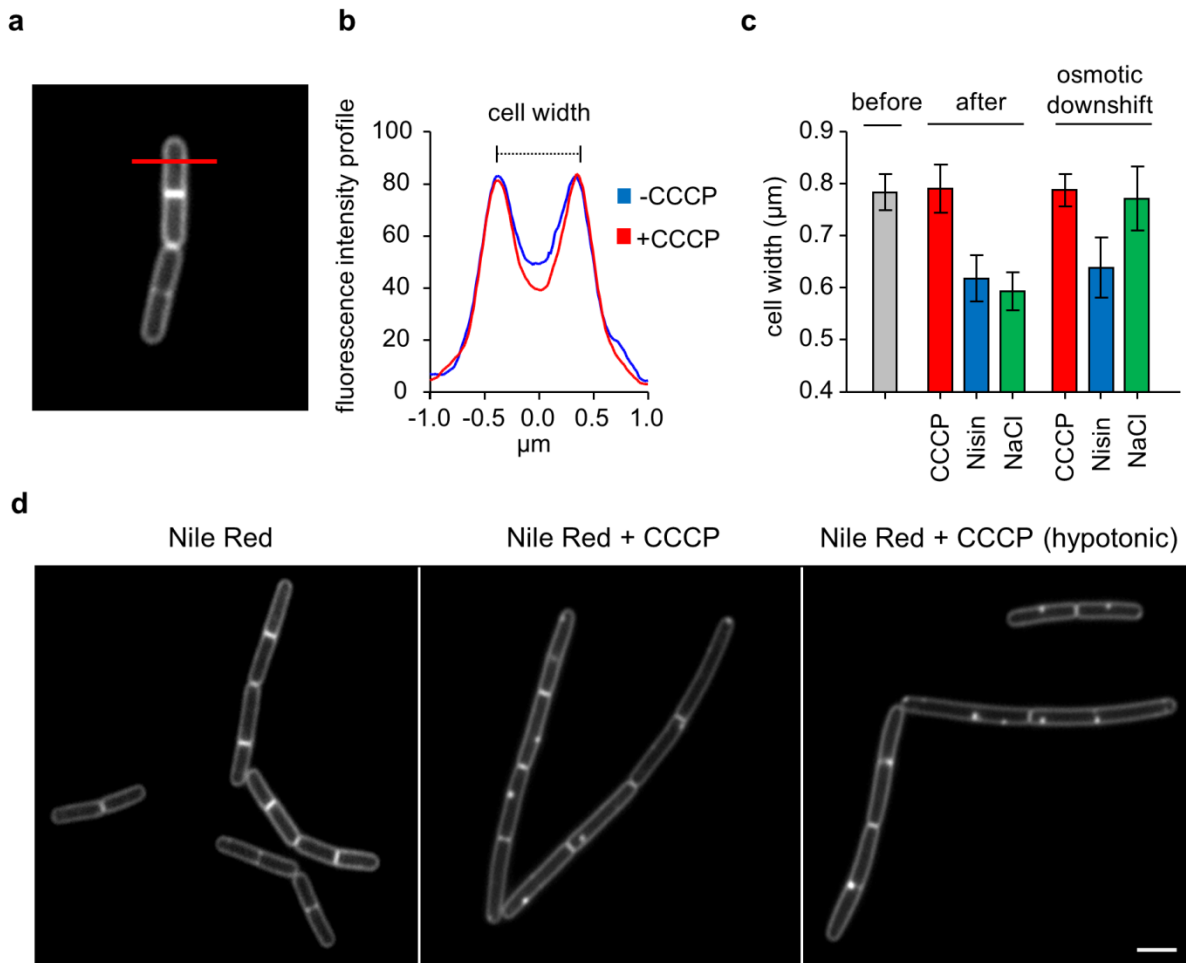
Nile Red foci are not caused by plasmolysis

Rapid loss of cell turgor as a result of CCCP treatment could result in invagination of the cell membrane. To test this possibility, we analysed the cell width that changes as a result of turgor changes. The cell width measurement was based on fluorescent intensity profiles along a line perpendicular to the cell axis (a), with cell width determined as the distance between maxima in membrane fluorescence (b). The average cell width and standard deviation of untreated cells, cells treated with CCCP, Nisin, and 0.5 M NaCl, and treated cells transferred to hypotonic medium (H2O) in order to recover turgor, was measured (n=50 cells) (c). Both Nisin (large pore forming antimicrobial peptide), and osmotic up-shock with 0.5 NaCl were used as positive control to evaluate the ability of our assay to reliably measure changes in cell turgor. No significant effect of CCCP treatment on cell turgor was detected. Finally, if

5

CCCP-dependent Nile Red-foci were caused by plasmolysis (membrane invagination), transfer to hypotonic environment, which recovers turgor, should reverse the membrane stain back to pre-treatment state. The Nile Red foci are not affected from the hypotonic challenge (d), further indicating that their formation is not related to plasmolysis caused by changes in cell turgor. Strain used: *B. subtilis* 168 (wild type). Scale bar, 2 μm.

Supplementary Figure 4
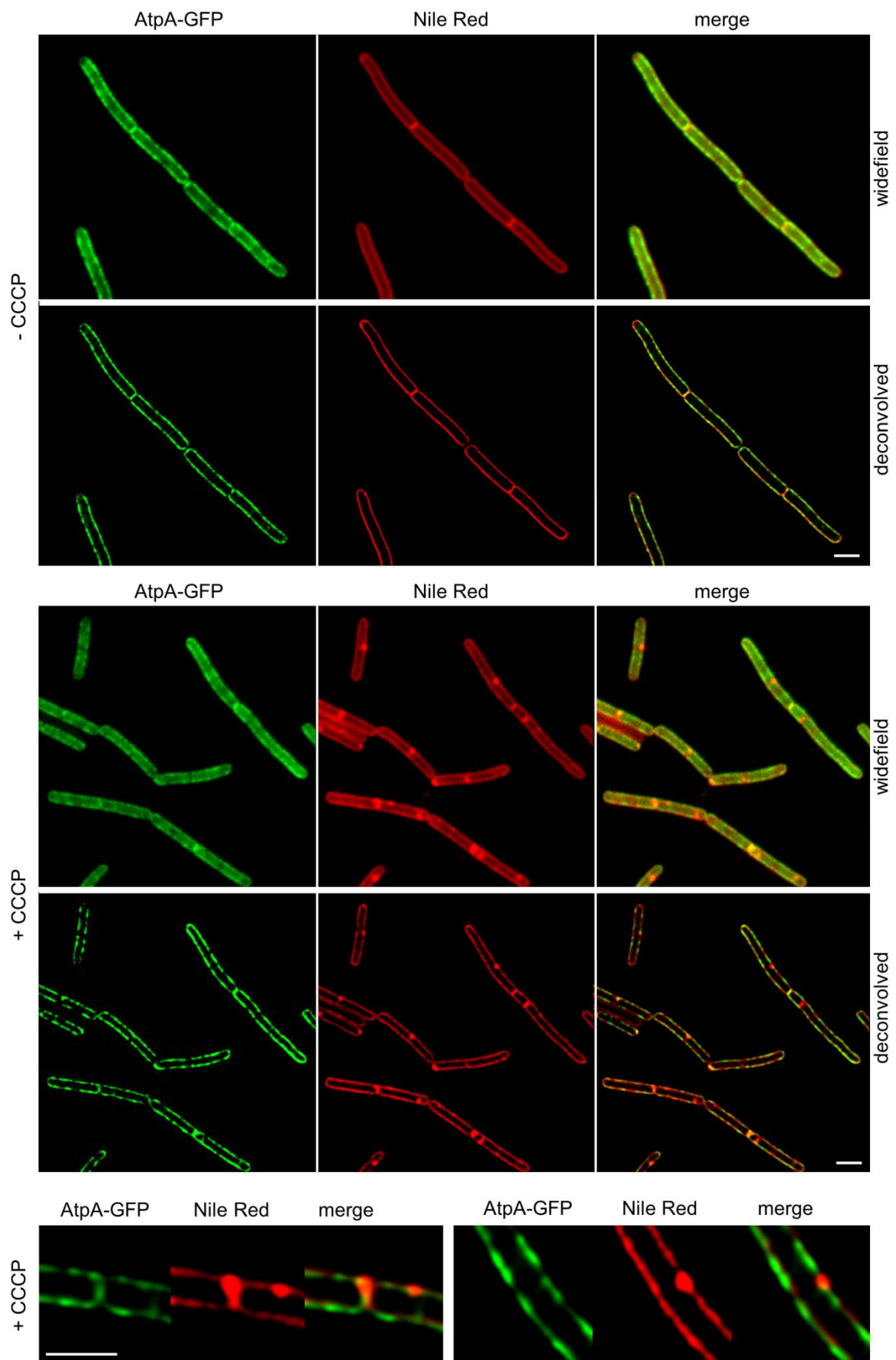
Nile Red foci are not caused by local invagination of the cell membrane

The irregularities in Nile Red membrane staining emerge within minutes, leaving very little time for the synthesis of excess membranes. To confirm that the Nile Red foci are not due to additional membrane layers, e.g. as a consequence of local invagination of the membrane, the localization of an integral membrane protein F_1F_o ATP synthase was determined using a GFP fusion protein (AtpA-GFP). Indeed, this protein does not show any enrichment in membrane areas where Nile Red cluster emerge upon CCCP treatment (middle panels, see lower panels for higher magnification). This rules out the presence of local membrane invaginations upon CCCP treatment. The images were captured as 200 nm optical sections. Both wide field images of the centre plane and the corresponding plane from deconvolved images are depicted in the absence and presence of CCCP. The reason that in some cases the Nile red stain appears to protrude into the cytoplasm is a consequence of high membrane fluorescence originating from slightly above and below the exact focal plane. Strain used: *B. subtilis* BS23 (*atpA-gfp*). Scale bar, 2 μm.
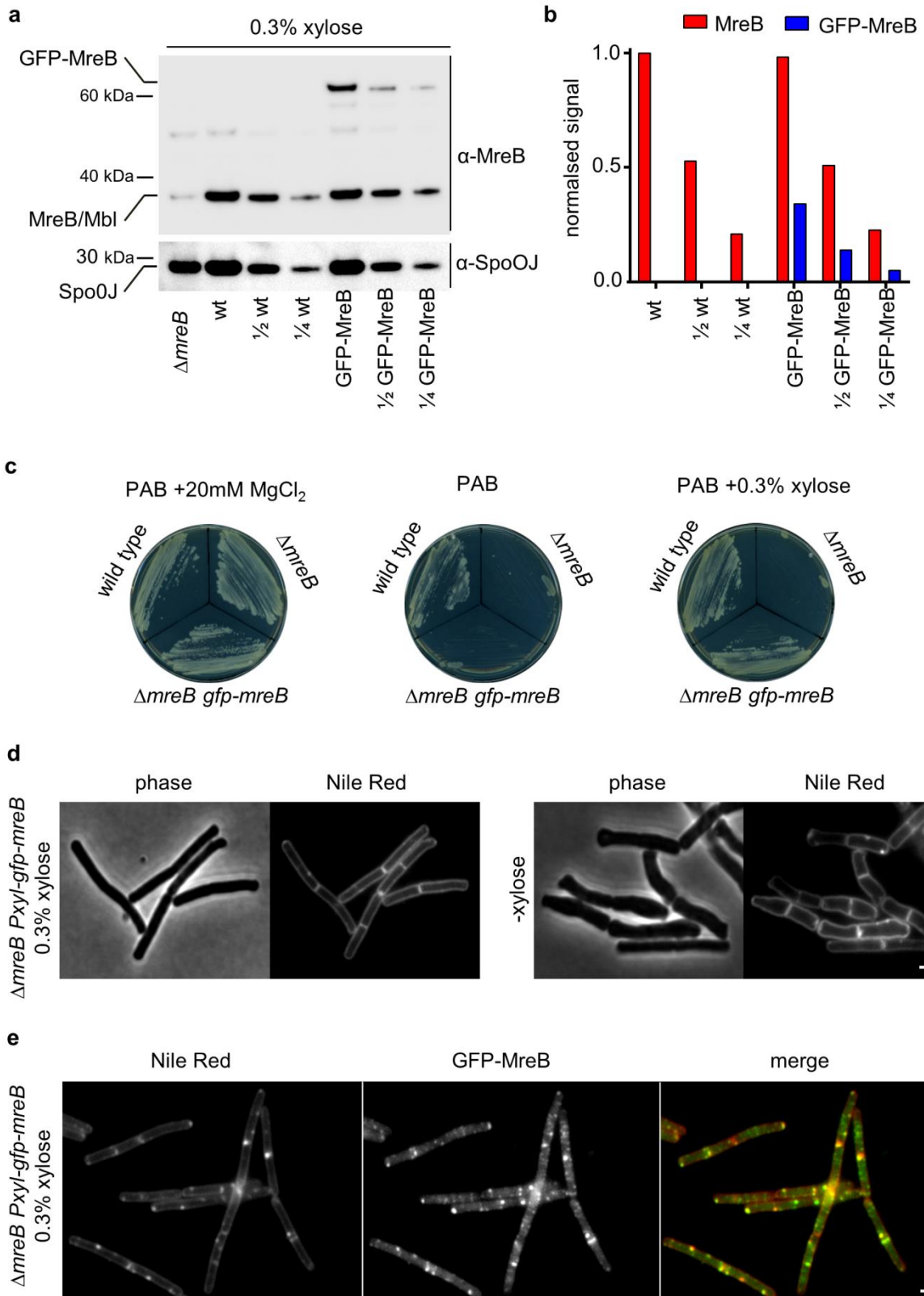
Supplementary Figure 5
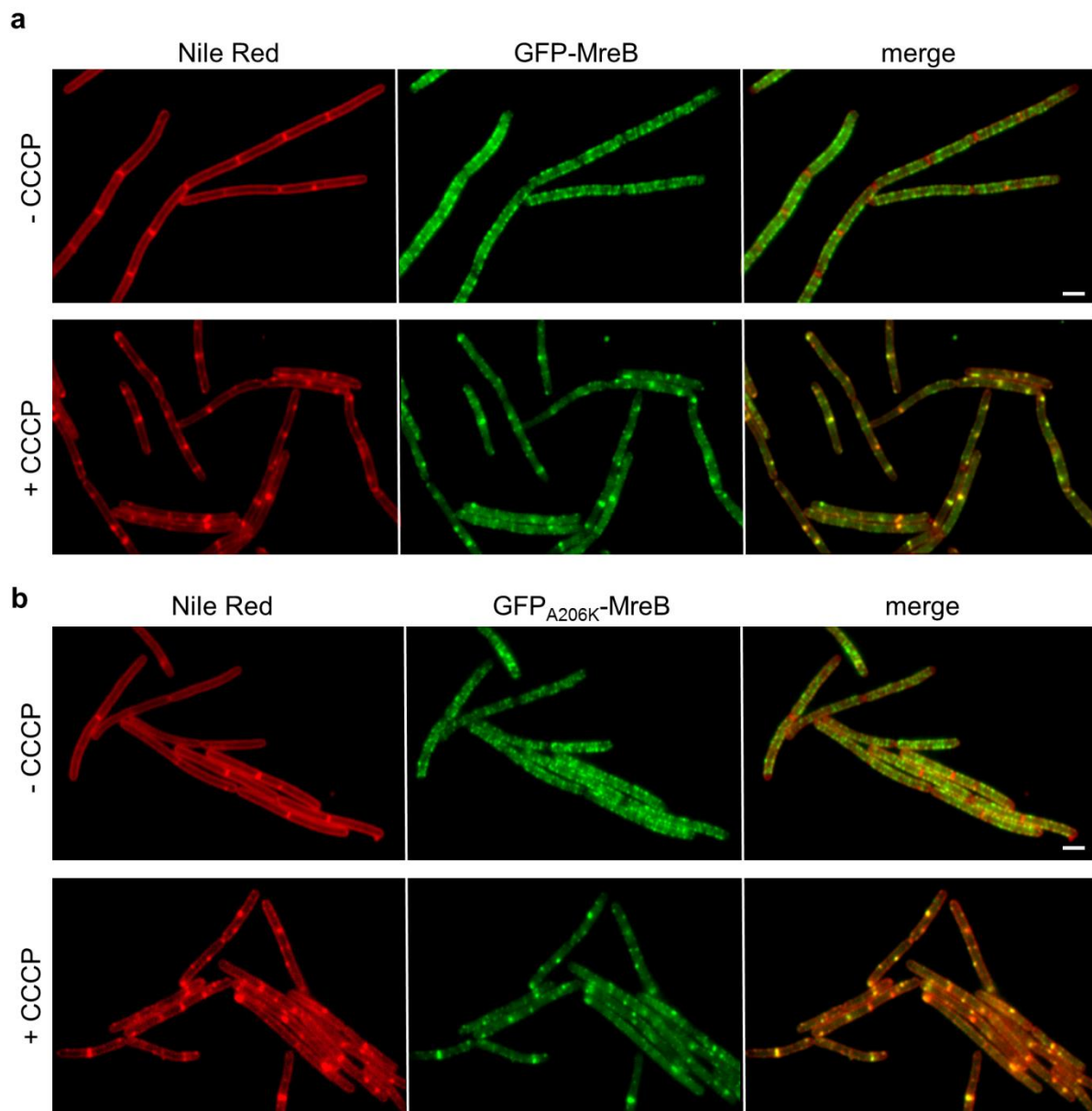
Disruption of the MreB cytoskeleton is accompanied by aberrant membrane stains

(a) Nile Red membrane stained *B. subtilis* cells (left panel) expressing GFP-MreB (middle panel), and merged images are depicted in the absence or presence of the proton ionophore CCCP. This is a larger field of cell shown in Fig. 1a. Strain used: *B. subtilis* YK405 (*gfp-mreB*). (b) Dimerization of GFP was recently shown to cause artificial clustering of certain GFP-fusion proteins (Landgraf *et al,* 2012). To verify that the localization and clustering of GFP-MreB is not influenced by this property, the experiments were repeated with a

monomeric GFP variant (GFP$_{A206K}$). This gave the same results (panel b). Nile Red membrane stains of *B. subtilis* cells (left panel) expressing GFP$_{A206K}$-MreB (middle panel), and merged images, are depicted in the absence or presence of the proton ionophore CCCP. The native localization of *B. subtilis* MreB, its delocalization upon CCCP-treatment, and the colocalization with Nile Red foci, is not influenced by the A206K mutation in GFP. Strain used: *B. subtilis* HS37 (*mgfp-mreB*). Scale bar, 2 μm.
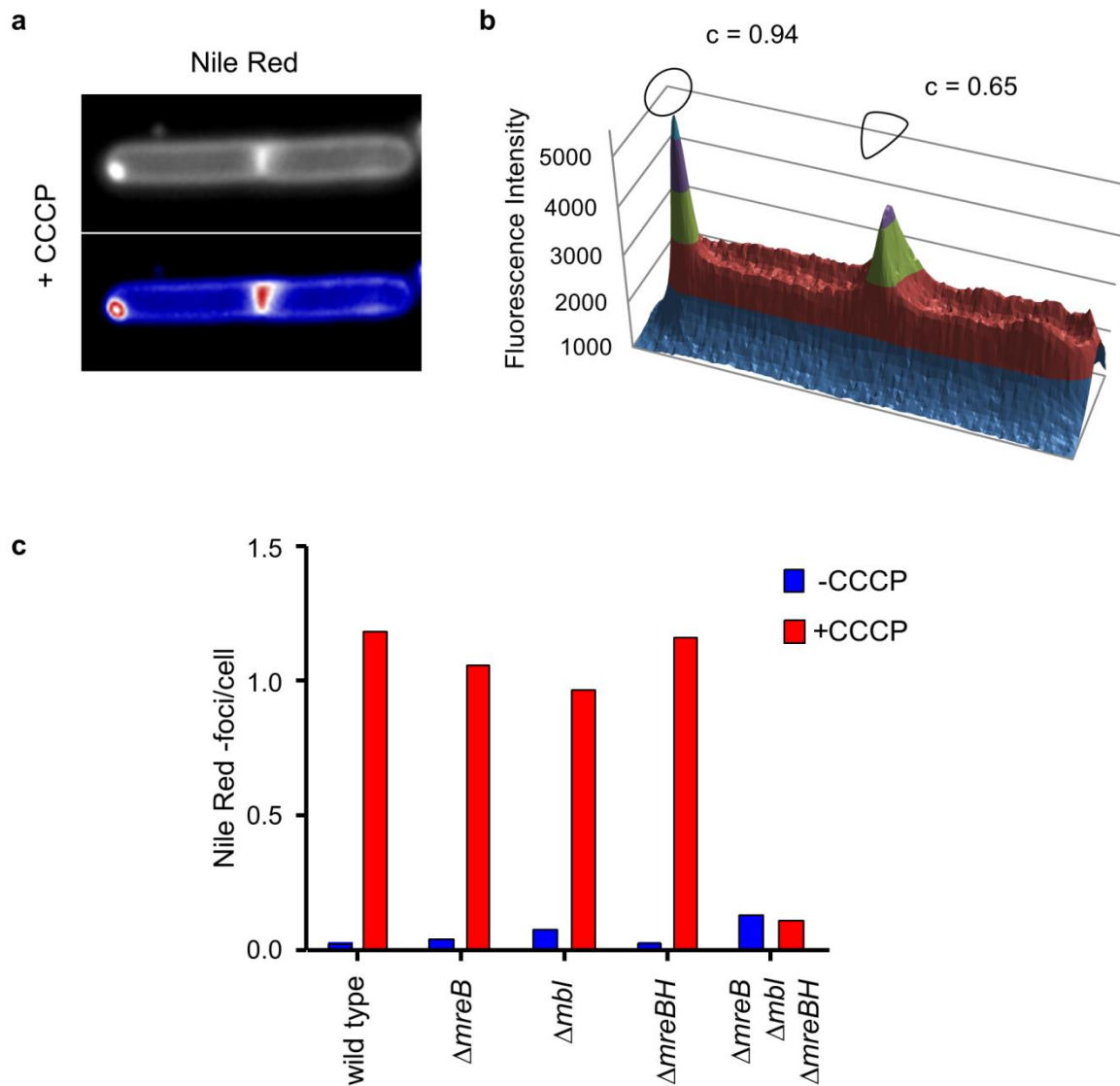
Supplementary Figure 6

a

0.3% xylose

GFP-MreB

60 kDa —

α-MreB

40 kDa —

MreB/Mbl

30 kDa —

α-SpoOJ

Spo0J

ΔmreB   wt   ½ wt   ¼ wt   GFP-MreB   ½ GFP-MreB   ¼ GFP-MreB

b

MreB   GFP-MreB

normalised signal

1.0

0.5

0.0

wt   ½ wt   ¼ wt   GFP-MreB   ½ GFP-MreB   ¼ GFP-MreB

c

PAB +20mM MgCl₂   PAB   PAB +0.3% xylose

wild type   ΔmreB

ΔmreB gfp-mreB

d

ΔmreB Pxyl-gfp-mreB
0.3% xylose

phase   Nile Red   phase   Nile Red

-xylose

e

ΔmreB Pxyl-gfp-mreB
0.3% xylose

Nile Red   GFP-MreB   merge

GFP-MreB is active and not overproduced

(a) The expression levels of *gfp-mreB* transcribed from the inducible Pxyl-promoter were compared with native levels of MreB using western blotting. Wild type cells inducing *gfp-mreB* (0.3% xylose, the maximal levels used in this manuscript) were analysed to allow a direct comparison. MreB was detected using polyclonal MreB antibodies. Detection of Spo0J was used as a loading control. To verify that the signals are not saturated, a serial dilution of the samples was performed. Please note that due to high sequence similarity, weak cross-reactivity with Mbl is present. Strains used: *B. subtilis* YK405 (*gfp-mreB*), and 3728 (Δ*mreB*). (b) Densitometric analysis of relative MreB signal intensities reveals that GFP-MreB levels are approximately 30% of the native MreB levels under these induction conditions. (c) GFP-MreB, induced with 0.3% xylose, is able to support growth under conditions in which MreB is essential (PAB-Agar plates without added $MgCl_2$) indicating that the fusion protein is active. (d) GFP-MreB, induced with 0.3% xylose, is able to rescue morphology phenotype of Δ*mreB* (PAB liquid medium, 3h after removal of 20 mM $MgCl_2$). Strain used: *B. subtilis* HS48 (*gfp-mreB*, Δ*mreB*). (e) In the absence of native MreB, GFP-MreB expressed at low levels in LB medium is delocalized by CCCP, and colocalize with Nile Red-foci. Strain used: *B. subtilis* HS48 (*gfp-mreB*, Δ*mreB*). Scale bar, 2 μm. Thus, the delocalization of GFP-MreB by CCCP, and the colocalization with Nile Red-foci, is not caused by overexpression of a non-functional MreB GFP-fusion. Scale bars, 2 μm.

Supplementary Figure 7

a

Nile Red

+ CCCP

b

c = 0.94

c = 0.65

Fluorescence Intensity

5000
4000
3000
2000
1000

c

Nile Red -foci/cell

1.5

1.0

0.5

0.0

■ -CCCP
■ +CCCP

wild type   ΔmreB   Δmbl   ΔmreBH   ΔmreB Δmbl ΔmreBH

Automated quantification of Nile Red foci –frequency

The frequency of CCCP-induced Nile Red-foci in different strain backgrounds was analysed using an automated detection scheme and ImageJ. (a) An initial screen was performed to identify membrane areas with fluorescent intensities 1.5 times above the average membrane signals, and area between 10 and 100 pixel^2. (b) The detected membrane areas were further divided based on circularity with values above 0.75 regarded as Nile Red –foci, and values below as septa (the presence of two membranes at septum result in higher fluorescence signals). (c) Finally, the frequency of Nile Red-foci was calculated based on manual cell

13

count of the corresponding image frames. The analysis of rod shaped cells was performed by capturing a single focal plane, and included 355-450 cells. Due to the large round shape of the Δ*mreB* Δ*mbl* Δ*mreBH* –cells, the analysis (190-210 cells) was performed with images captured as 500 nm optical sections. Strains used: *B. subtilis* 168 (wild type), 3728 (Δ*mreB*), 4261 (Δ*mbl*), 4262 (Δ*mreBH*), and 4277 (Δ*mreB*, Δ*mbl*, Δ*mreBH*).

Supplementary Figure 8
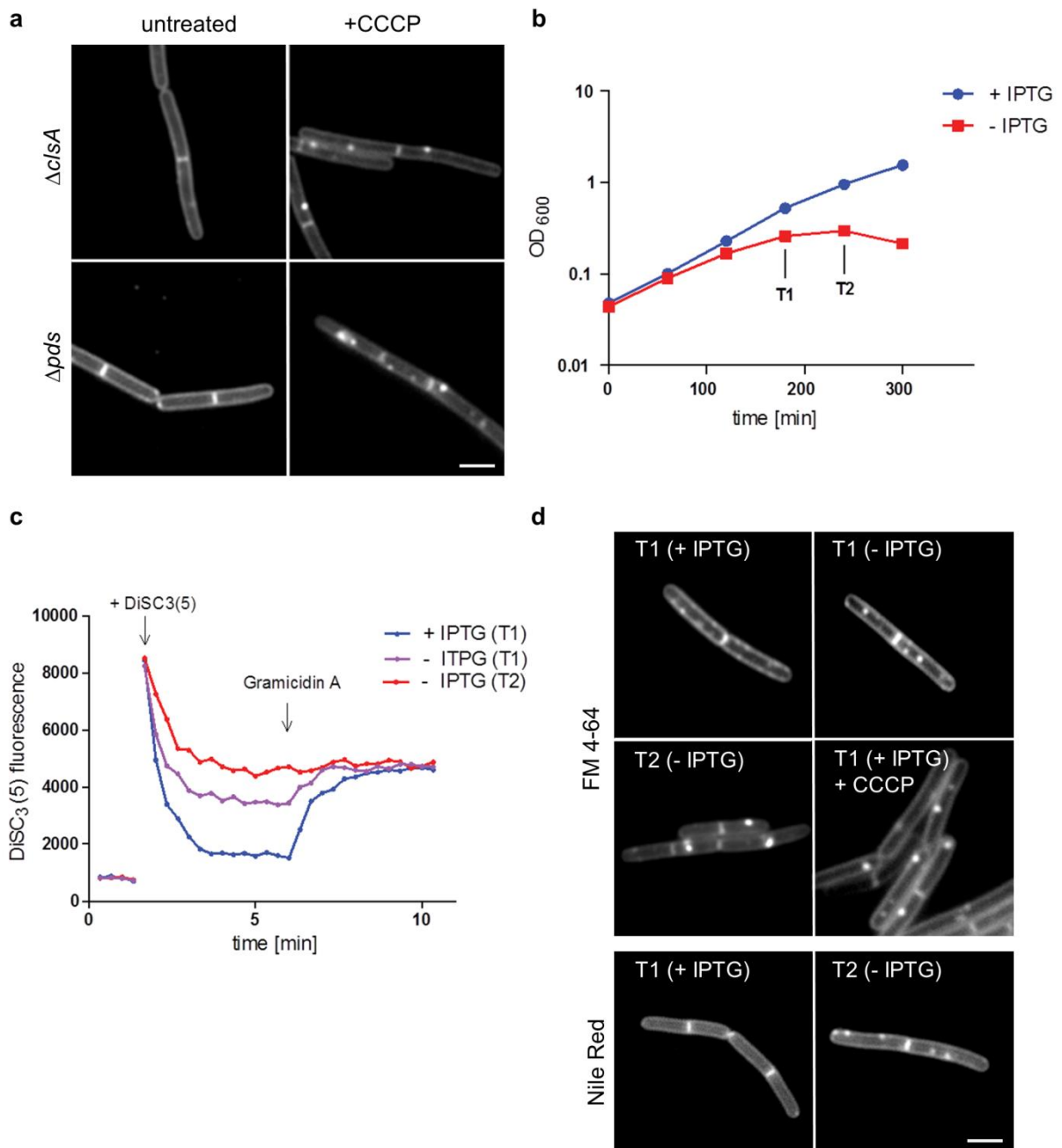
CCCP induced change in the fluorescent membrane stain is independent of lipid head groups

(a) Appearance of Nile Red foci after addition of CCCP in *B. subtilis* strains deficient for cardiolipin (Δ*clsA*) or phosphatidyl ethanolamine (Δ*psd*). Strains used: *B. subtilis* HB5347 (Δ*clsA*) and HB5343 (Δ*psd*). Scale bar, 2 μm. (b) An irregular fluorescent stain in *B. subtilis* cells that weakly resembles a helical pattern has been reported for the membrane dye FM 4-

64 [5, 6]. This was interpreted as phosphatidyl-glycerophosphate (PG) -enriched helical domains, since these structures coalesce when PG is depleted [5]. PG is essential and the most abundant lipid species. Depletion of PG synthase (PgsA) results in an inhibition of growth as shown in panel B (growth curves in the presence (+ IPTG) and absence (- IPTG) of *pgsA*-expression). Time points in which samples were withdrawn for membrane potential measurements (panel C), and microscopy (panel D) are highlighted as T1 and T2. (c) Depletion of PG coincides with dissipation of the membrane potential due to destabilisation of the lipid bilayer barrier function. The cellular membrane potential levels were measured using the fluorescent membrane potential-sensitive dye $DiSC_3(5)$ as described before [1]. Briefly, in the presence of a transmembrane potential the membrane permeable cationic dye $DiSC_3(5)$ accumulates in the cytoplasm. The resulting high local concentration results in quenching of the fluorescence within the cytoplasm. Upon dissipation of the membrane potential with 1 μM Gramicidin A, the dye is released back into the medium. (d) As described before [5], depletion of PgsA results in a change from a weakly helical FM 4-64 membrane stain (T1 + IPTG) to a strongly clustered signal (T1 and T2 − IPTG). However, these irregularities in FM 4-64 stain are also triggered by direct dissipation of the membrane potential with CCCP, even when *pgsA* is expressed (T1 + IPTG and CCCP). Identical clustering upon PgsA depletion (T2 − IPTG) is observed in cells stained with Nile Red as well. Scale bar, 2 μm. Strain used for B-D: *B. subtilis* BFA2809 (*Pspac-pgsA*).. In conclusion, the change of the fluorescent FM 4-64 pattern is due to delocalization of MreB caused by dissipation of membrane potential, and this lipid dye is not an indicator for PG-enriched membrane domains.
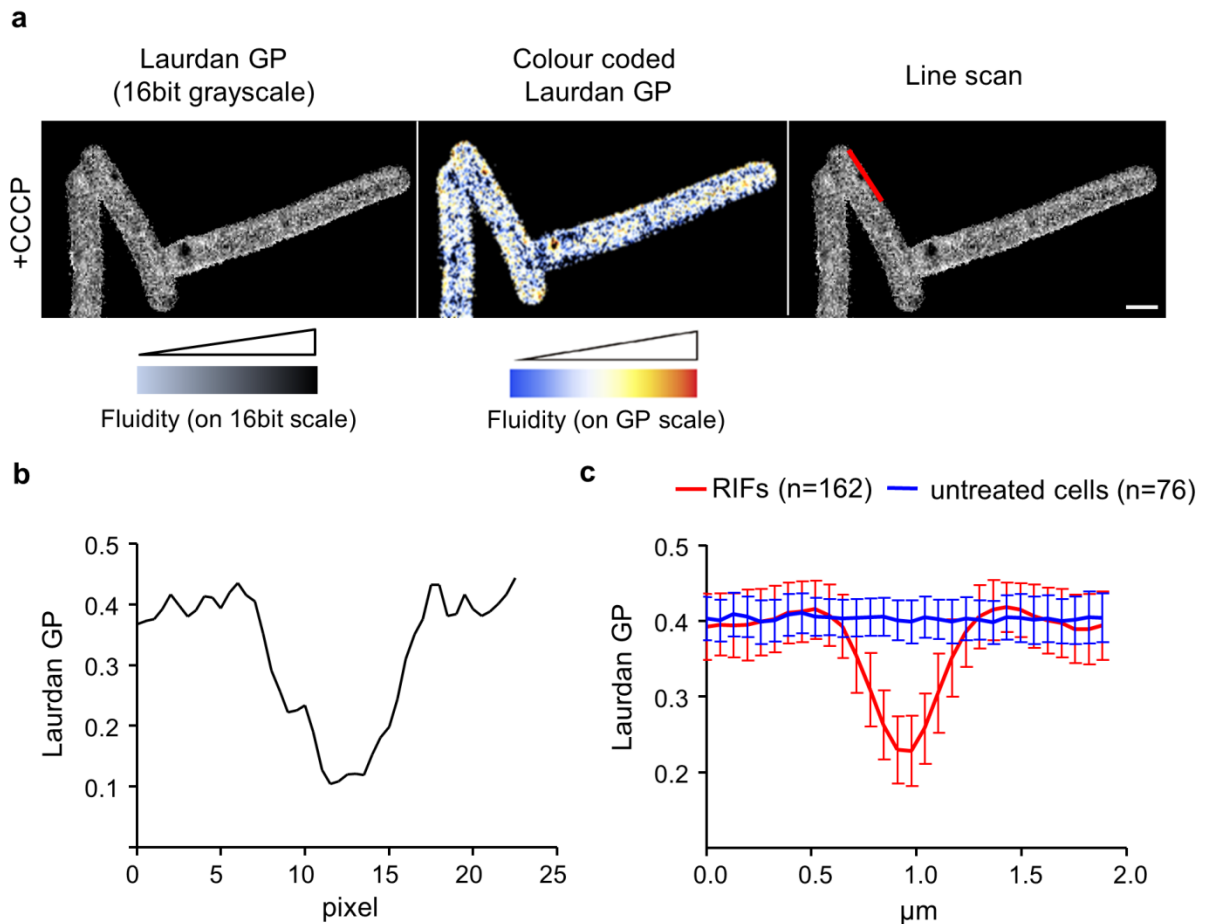
Supplementary Figure 9
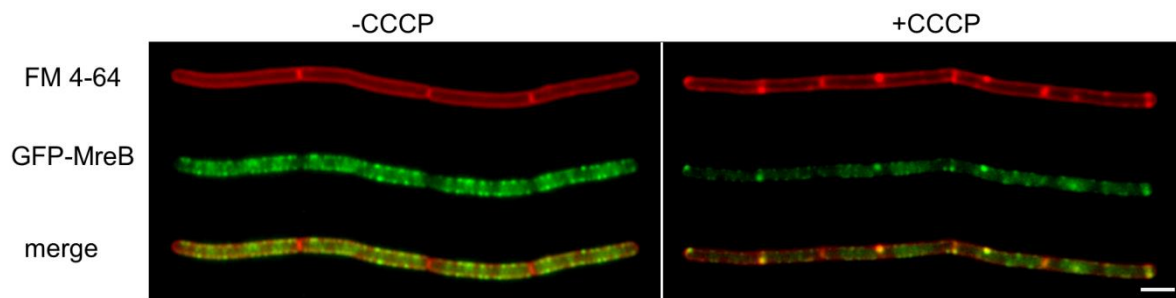
The FM 4-64 foci colocalize with GFP-MreB upon CCCP treatment

FM 4-64 stained *B. subtilis* cells (upper panels) expressing GFP-MreB (middle panels), and merged images (right panels) are depicted in the absence or presence of the proton ionophore CCCP. Strain used: *B. subtilis* YK405 (*gfp-mreB*). Scale bar, 2 μm.

Supplementary Figure 10

Statistical analysis of changes in local membrane fluidity

To analyse the statistical significance of the detected local changes in membrane fluidity measured as Laurdan generalised polarisation (GP), the RIF-associated change in Laurdan GP was measured using a line scan along the length axis of the cell membrane, centred at RIFs. (a) The analysis was carried out from images in which the Laurdan GP is presented in 16 bit scale (from 0 to 65,536), followed by conversion to GP scale (from -1 to +1). The individual intensity profiles (b) were averaged and are (c) presented as mean and standard deviation for 162 RIFs caused by CCCP treatment, and 76 randomly selected membrane areas of untreated cells. Scale bar, 2 µm. In conclusion, incubation with CCCP generates membrane areas with a significant reduction in 'Laurdan Generalised Polarisation', which indicates an increase in local membrane fluidity.
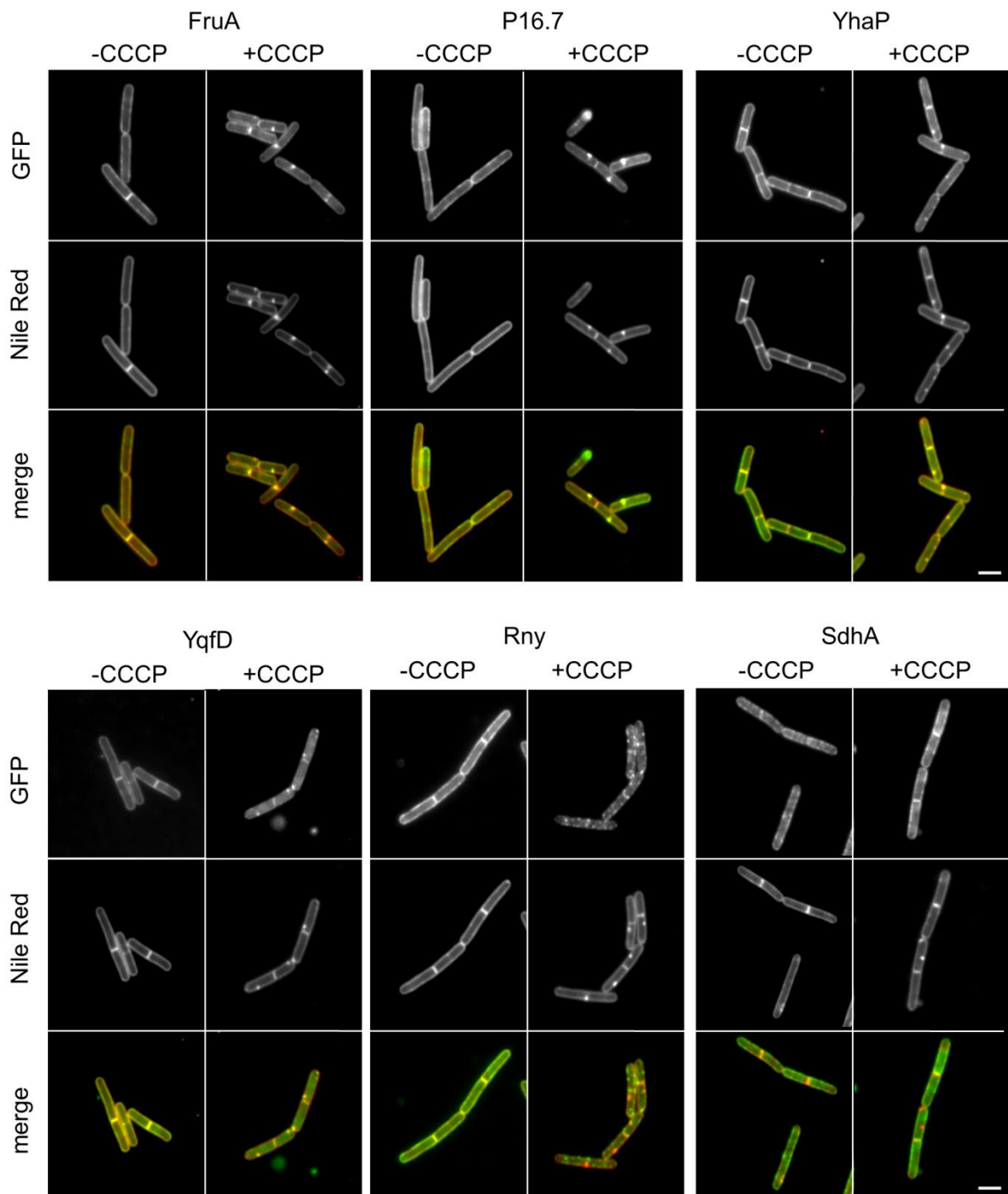
Supplementary Figure 11

a

| DiI-C12 | GFP-MreB | merge |

b

c

| ΔmreB, Δmbl, ΔmreBH | ΔmreC | ΔmreD |
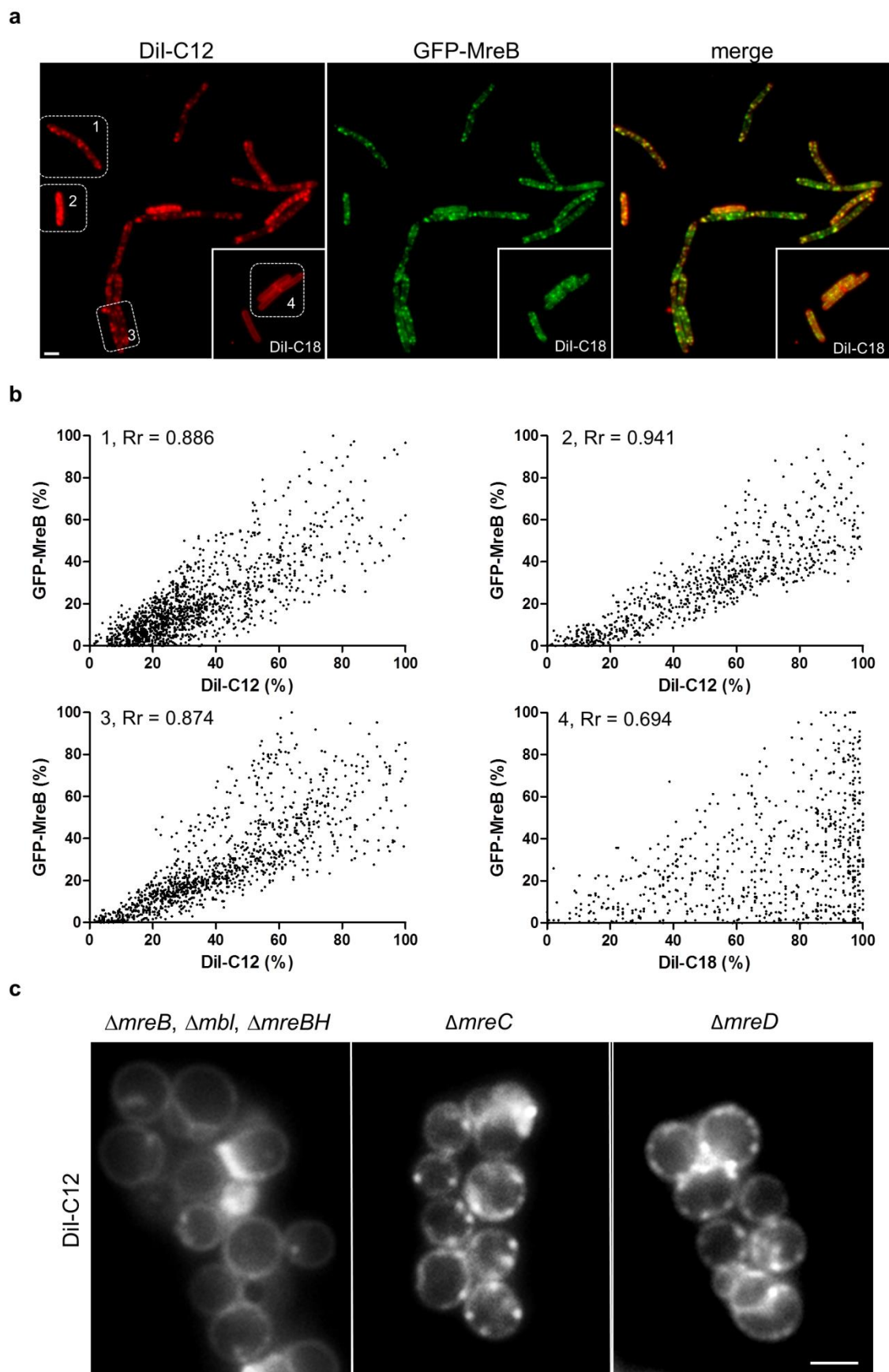
Colocalization of DiI-C12 stained RIFs and GFP-MreB

(a) A field of DiI-C12 membrane stained *B. subtilis* cells (left panel) expressing GFP-MreB (middle panel), and merged images (right panel) is depicted. For comparison, captions of DiI-C18 stained cells are shown in the lower right corners. Strain used: *B. subtilis* YK405 (*gfp-mreB*). This panel shows a larger field of cells shown in Fig. 4b. (b) Fluorescence intensity correlation graphs are shown for 4 random cells in panel B. The graphs display a pixel by pixel intensity correlation between DiI, and GFP-MreB fluorescence. For the analysis, the fluorescence images were background subtracted, and the intensities equalized by conversion into 8 bit images with lowest intensities represented as 0, and highest pixel values as 255. The analyses were carried out using ImageJ "Intensity Correlation Analysis" plugin (Tony Collins, Wright Cell Imaging Facility, Canada) based on Li *et al*, 2004 [7]. The relative intensities are represented as % of the maximal values of the corresponding image fields. Pearson's correlation coefficients, which indicates the significance of correlation on a scale of -1 (full exclusion) to $+1$ (full correlation), are calculated (Rr). The average Pearson's correlation coefficient for DiI-C12 and GFP-MreB in 19 individual cells was 0.859, indicating a high level of spatial correlation. Importantly, the correlation for DiI-C18 stained cells is significantly lower (Rr = 0.69). It should be mentioned that some fluorescence correlation between DiI-C18 and GFP remains since both DiI-C18 and MreB are present in the cell membrane. (c) DiI-C12 fluorescence images of *B. subtilis* Δ*mreC* and Δ*mreD* cells, and cells that lack the three MreB-homologs (Δ*mreB*, Δ*mbl*, Δ*mreBH*). This is a larger field of cells shown in Figure 5a. Strains used: *B. subtilis* 3481 (Δ*mreC*), 4311 (Δ*mreD*), 4277 (Δ*mreB, Δmbl, ΔmreBH, ΔrsgI*). Scale bar, 2 μm

Supplementary Figure 12

Colocalization of CCCP-induced membrane protein clusters with Nile Red

CCCP induces clustering of several membrane proteins (FruA, P16.7, YhaP, YqfD, and Rny), whereas the localization of other proteins (SdhA, for AtpA see Supplementary Fig. 4) remains unaffected. In case of FruA, P16.7, YhaP and YqfD, the induced clusters colocalize with Nile Red membrane foci. The delocalization of Rny follows a different pattern. In this

case, rather than forming few clusters that overlap with Nile Red-foci, a large number of non-colocalizing clusters are formed. Strains used: *B. subtilis* 3569 (*rny-gfp*), FruA-GFP, 110WA (*p16.7-gfp*), *yhaP-gfp, yqfD-gfp*, and BS112 (*sdhA-gfp*). Scale bar, 2 μm

Supplementary Figure 13
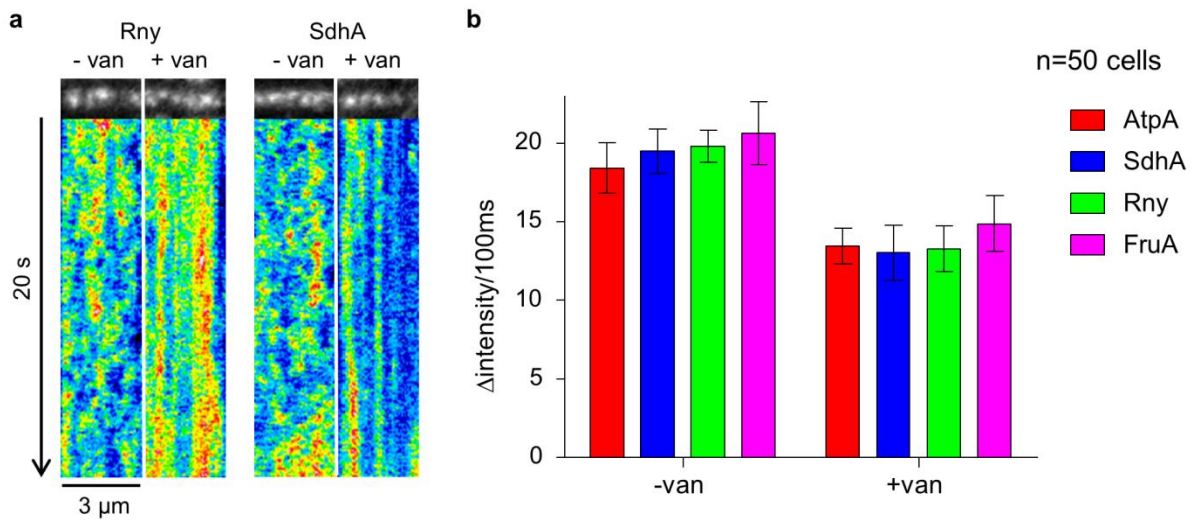
**Quantification of vancomycin-inhibited membrane protein mobility**

(a) Kymographs visualizing the diffusion of RNaseY (Rny) and Succinate dehydrogenase (SdhA), in the absence and presence of vancomycin, which blocks MreB movement. Time lapse series with 20 s length and 100 ms time resolution were acquired using TIRF microscopy. See movie S5 for corresponding raw image series. Strains used: *B. subtilis* 3569 (*rny-gfp*) and BS112 (*sdhA-gfp*). (b) The statistical significance of the observed reduction in mobility of membrane proteins upon inhibition of MreB-movement was confirmed using fluorescence intensity fluctuation analysis. The movement of a membrane protein with a heterogeneous distribution pattern results in fluctuation of the fluorescence intensity for a given pixel over time, with larger fluctuations reflecting higher mobility. This property also forms the fundamental basis for fluorescence correlation spectroscopy (FCS). We analysed the average time-dependent change in pixel intensity for 50 individual cells in the presence and absence of vancomycin. The pixel intensities were recorded as an average intensity of 3 neighbouring pixels following a 31 pixel long line along the length axis of the cell. The values were normalised through conversion into 8 bit image, which defines the highest intensity values as 256, and the lowest as 0. The intensity fluctuation for each pixel was

calculated as $\Delta I = |I(t_n) - I(t_{n+1})|$ for 200 time points (100 ms time resolution). Finally, the individual ΔI -values for 200 time points, 31 pixel values, and 50 cells were averaged and are represented as mean and standard deviation. A clear reduction of intensity fluctuation is observed for cells treated with vancomycin, indicating a significant reduction in mobility. Strains used: *B. subtilis* 3569 (*rny-gfp*), FruA-GFP, 110WA (*p16.7-gfp*), *yhaP-gfp, yqfD-gfp*, BS112 (*sdhA-gfp*), and BS23 (*atpA-gfp*).

Supplementary Figure 14

a

b
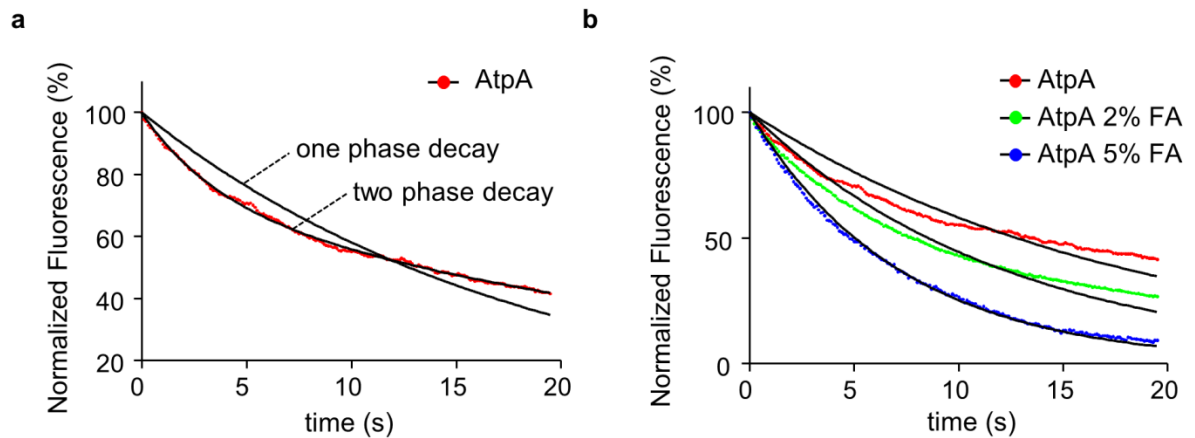
	k (1/s)	SEM	R²	n (cells)
AtpA	5.44E-02	6.5E-04	0.896	32
AtpA 2% FA	8.12E-02	7.3E-04	0.959	39
AtpA 5% FA	1.38E-01	4.7E-04	0.997	45

c
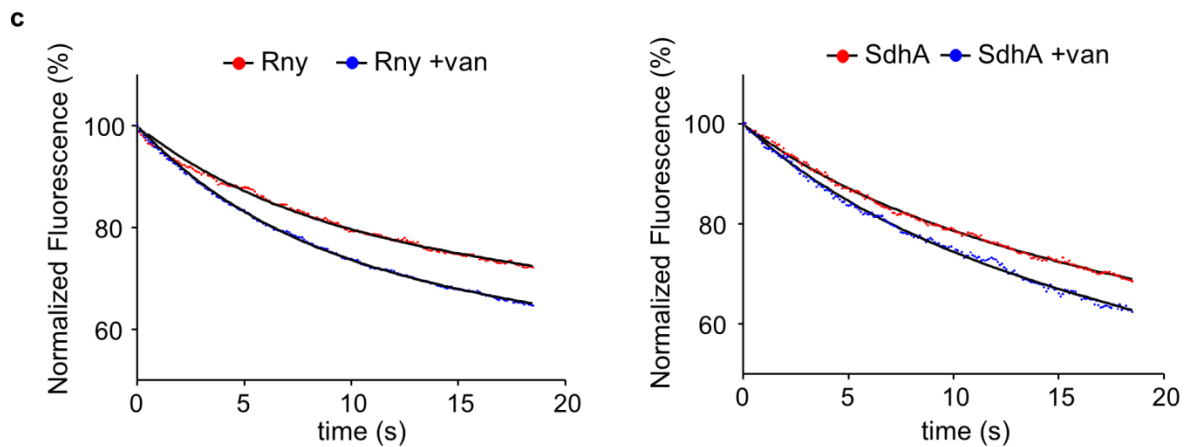
d

	k (1/s)	SEM	R²	n (cells)
FruA	6.96E-03	4.6E-04	0.988	47
FruA + vancomycin	8.84E-03	3.4E-04	0.997	42
Rny	4.65E-03	3.1E-04	0.993	51
Rny + vancomycin	6.35E-03	1.7E-04	0.999	48
AtpA	5.97E-03	1.9E-04	0.996	52
AtpA + vancomycin	9.43E-03	2.1E-04	0.998	55
SdhA	11.4E-03	2.0E-04	0.998	36
SdhA + vancomycin	14.9E-03	3.3E-04	0.997	37

Quantification of bleaching kinetics

(a) The normalised and background-subtracted GFP fluorescence intensity (AtpA-GFP) follows a biexponential decay from 100 to 0 ($y=y0*e^{(-kfast*x)}+y0*e^{(-kslow*x)}$), with fast rate constant associated with bleaching of GFP within the reach of the evanescent light, and slow rate constant determined by diffusion limited bleaching of the whole cell fluorescence. (b) To verify that biexponential decay is diffusion limited, and to analytically determine the rate constant for direct GFP-bleaching, unfixed samples were compared with samples in which the mobility of the membrane protein was reduced by chemical fixation with formaldehyde. In contrast to unfixed and mildly fixed (2% FA) samples, strong fixation (5% FA) results in bleaching kinetics which follow monoexponential decay ($y=y0*e^{(-k*x)}$) with a single rate constant (0.1378 1/s). (c-d) The analytically determined fast rate constant was used to fit the biexponential decay functions of Fructose permease (FruA), F_1F_o ATP synthase (AtpA) (see Fig. 8b), RNaseY (Rny), and Succinate dehydrogenase (SdhA) (shown here). In all cases, a significant increase in diffusion-limited slow rate constant was observed, which indicates a reduced exchange of proteins between the TIRF-illuminated area, and rest of the cell surface, thus, reduced diffusion rates. Strains used: *B. subtilis* BS23 (*atpA-gfp*), BS112 (*sdhA-gfp*), FruA-GFP, and 3569 (*rny-gfp*).

Supplementary Figure 15
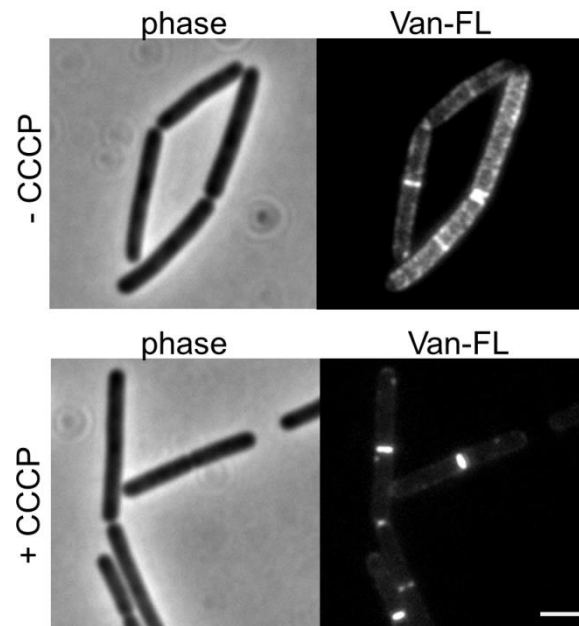
**Lipid II levels in the lateral cell wall are reduced by CCCP**

Lipid II was stained with fluorescent vancomycin in the absence (left panels) and presence (right panels) of CCCP. In uninhibited cells undergoing cell division and elongation, Lipid II clusters at sites of active cell wall synthesis. The local enrichment of Lipid II in the cylindrical part of the cell (lateral cell wall) requires MreB [8]. Upon CCCP addition, the lateral clusters of Lipid II disappear whereas the septal staining remains unaffected. Strain used: *B. subtilis* 168 (wild type). Scale bar, 2 μm

Supplementary Figure 16

a
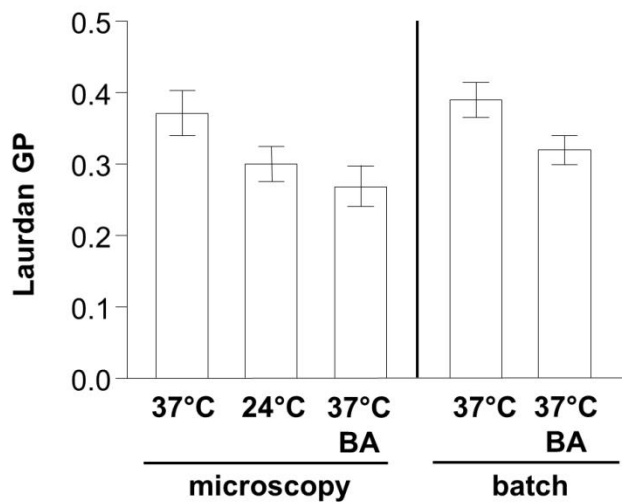
b
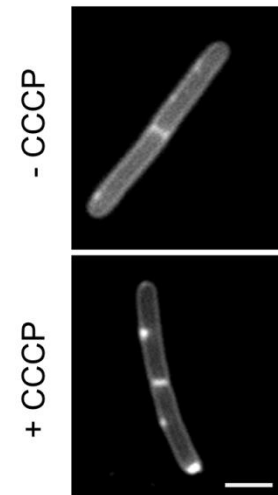
c
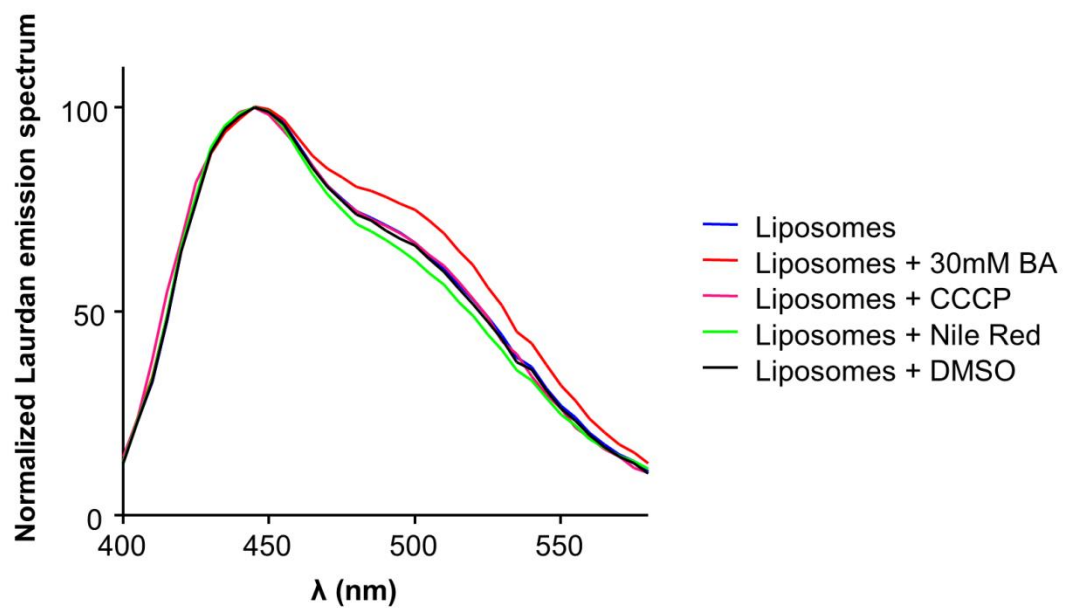
Comparison of Laurdan-based cell membrane fluidity measurements using fluorescence microscopy or fluorometric batch assays, and the influence of compounds on spectral properties of Laurdan

(a) For microscopic analyses, *B. subtilis* cells were grown at 37 ℃ or 24 ℃, followed by measurements at 24 ℃. In addition, the membrane fluidity was increased (decrease in Laurdan GP) by addition of 30 mM membrane fluidizer benzyl alcohol (BA). The fluidities

of 70 individual cells were analysed. For batch measurements, the fluidity was determined fluorometrically using cultures that were grown at 37 ºC and incubated for 2 min in the presence or absence of the membrane fluidizer benzyl alcohol (BA). The diagram depicts the average and standard deviation of 3 separate samples. Strain used: *B. subtilis* HB5134 (Δ*des*). (b) The lipid desaturase Des is responsible for rapid unsaturation of phospholipids. As a result of Des activity, elevated levels of fluid lipid species are formed upon cold shock. The formation of CCCP dependent Nile Red foci was independent of Des, indicating that local formation of unsaturated lipid species by Des is not responsible for the formation of RIFs. Strain used: *B. subtilis* HB5134 (Δ*des*). Scale bar, 2 μm (c) As an additional control, we verified that the compounds used in combination with Laurdan do not interfere with the spectral properties of Laurdan. For this, the emission spectrum of Laurdan embedded in liposomes was recorded. The spectra are an average of 3 independent wavelength scans. No significant changes in Laurdan emission spectrum were detected for CCCP, Nile Red, or DMSO (solvent used for CCCP and Nile Red) in the concentrations used in this manuscript. In addition, the positive spectral shift upon addition of 30 mM membrane fluidizer benzyl alcohol (BA) is shown. We conclude that neither CCCP, nor Nile Red interferes with the ability of Laurdan to detect changes in membrane fluidity.

Supplementary Figure 17
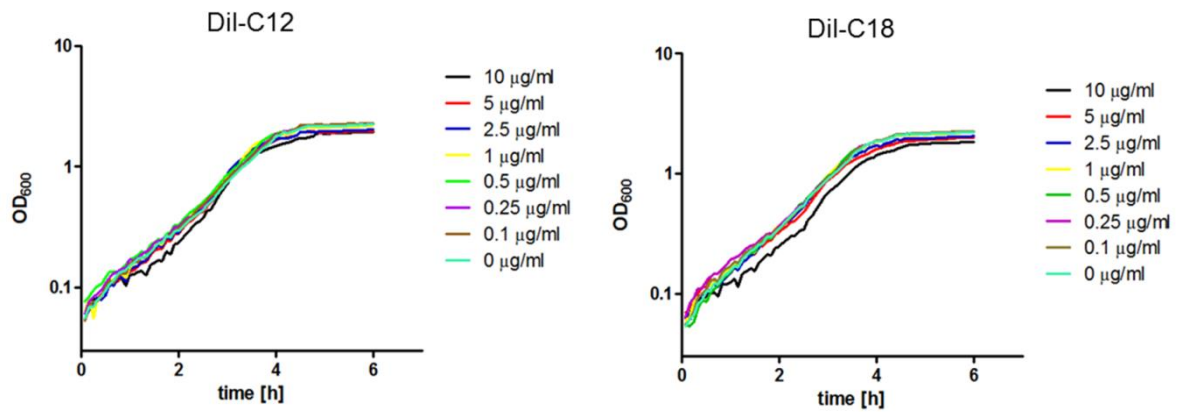
B. subtilis growth is not inhibited by DiI-C12 or DiI-C18

B. subtilis wild type cells were grown in microtiter plates with increasing concentrations of DiI-C12 or DiI-C18. The concentration of the solvent DMSO was maintained constant at 1%. No growth inhibitory effect was detected with 2-4 -fold higher concentrations than used for staining cell membranes (2.5-5 µg/ml).

SUPPLEMENTARY TABLES

Supplementary Table 1: Fatty acid profile, and changes in membrane fluidity of Δ*mre* strains

Fatty acid	wild type	Δ*rsgI*	Δ*mreC*	Δ*mreB**
$C_{14:0}$	**1.2** ±0.11	**1.0** ±0.00	<1	<1
$C_{14:0}$ *iso*	**1.7** ±0.21	**1.7** ±0.03	<1	<1
$C_{15:0}$ *iso*	**20.8** ±1.11	**19.6** ±0.17	**13.5** ±0.04	**16.7** ±0.01
$C_{15:0}$ *anteiso*	**37.6** ±2.42	**35.2** ±0.40	**37.4** ±0.08	**36.3** ±0.03
$C_{16:0}$	**6.5** ±0.25	**6.6** ±0.07	**7.0** ±0.04	**6.0** ±0.01
$C_{16:0}$ *iso*	**4.1** ±0.09	**4.6** ±0.01	**3.0** ±0.00	**2.3** ±0.02
$C_{17:0}$ *iso*	**11.2** ±0.95	**12.3** ±0.31	**14.7** ±1.44	**17.5** ±0.00
$C_{17:0}$ *anteiso*	**10.6** ±0.86	**11.0** ±0.26	**17.9** ±0.31	**16.6** ±0.03
$C_{18:0}$	**1.4** ±0.17	**1.5** ±0.09	**2.2** ±0.07	**1.6** ±0.02
$C_{18:1}$	**3.2** ±0.45	**3.3** ±0.04	<1	<1
sum	98.1 %	96.8 %	95.7 %	97.1 %
C17/C15	**0.37** ±0.05	**0.42** ±0.01	**0.64** ±0.01	**0.65** ±0.01
iso/anteiso	**0.78** ±0.03	**0.83** ±0.01	**0.57** ±0.00	**0.69** ±0.00
Laurdan GP	**0.44** ±0.02	**0.44** ±0.01	**0.43** ±0.02	**0.35** ±0.02

The fraction of fatty acids which contribute to more than 1% of the overall fatty acid content are presented as mean and standard deviation of duplicate measurements. The corresponding *in vivo* Laurdan GP values are presented as mean and standard deviation of three independent measurements. Strains used: *B. subtilis* 168 (wild type), 4264 (Δ*rsgI*), 3481 (Δ*mreC*), 4277/Δ*mreB** (Δ*mreB*, Δ*mbl*, Δ*mreBH*, Δ*rsgI*).

Supplementary Table 2: Strains

Strain	Genotype/Properties	Induction	Source
B. subtilis 168	*trpC2* wild type	-	9
B. subtilis HS13	*ery atpB:pMutin4*	-	1
B. subtilis 3728	*Ωneo3427 ΔmreB*	-	10
B. subtilis 4261	*cat Δmbl*	-	11
B. subtilis 4262	*ery ΔmreBH*	-	11
B. subtilis 4277	*Ωneo3427 ΔmreB Δmbl::cat*	-	11
	ΔmreBH::erm Ω(neo::spc) ΔrsgI		
B. subtilis 4264	*ΔrsgI::spc*	-	11
B. subtilis YK405	*spc amyE::Pxyl-gfp-mreB*	0.1-0.3 % xylose	12
B. subtilis HS37	*spc amyE::Pxyl-mgfp-mreB*	0.1 % xylose	this work
B. subtilis HS48	*spc amyE::Pxyl-gfp-mreB*	0.3% xylose	this work
	Ωneo3427 ΔmreB		
B. subtilis RD159	*neo rodA::Pspac-rodA*	0-100 μM IPTG	R. Daniel, unpublished
B. subtilis BS23	*cat atpA-gfp:Pxyl-'atpA*	0.5% xylose	13
B. subtilis BS112	*cat sdhA-gfp:Pxyl-'sdhA*	0.5% xylose	13
B. subtilis 110WA	*spc amyE::Pxyl-p16.7-gfp*	0.3% xylose	14
B. subtilis FruA-GFP	*spc amyE::Pxyl-fruA-gfp*	1% xylose	15
B. subtilis YhaP-GFP	*spc amyE::Pxyl-yhaP-gfp*	1% xylose	15
B. subtilis YqfD-GFP	*spc amyE::Pxyl-yqfD-gfp*	1% xylose	15
B. subtilis 3569	*spc amyE::Pxyl-rny-gfp*	1% xylose	16
B. subtilis HB5347	*tet ΔclsA*	-	17
B. subtilis HB5343	*ery Δpsd*	-	17
B. subtilis HB5134	*spc Δdes*	-	18
B. subtilis HS31	*ery mreD:pMutin4 (mreD1-172)*	-	this work
B. subtilis HS32	*ery mreD:pMutin4 (mreD1-157)*	-	this work
B. subtilis HS33	*ery spc mreD:pMutin4 (mreD1-172)*	0.1% xylose	this work
	amyE::Pxyl-gfp-mreB		
B. subtilis HS34	*ery spc mreD:pMutin4 (mreD1-157)*	0.1% xylose	this work
	amyE::Pxyl-gfp-mreB		
B. subtilis HS35	*spc neo amyE::Pxyl-gfp-mreB ΔmreBCD*	0.3% xylose	this work
B. subtilis BFA2809	*ery pgsA::pMutin4*	0-100 μM IPTG	19
B. subtilis HS36	*spc neo amyE::Pxyl-gfp-mreB*	0.3% xylose	
	rodA::Pspac-rodA	0-100 μM IPTG	this work
B. subtilis HS38	*tet amyE::Pxyl-rny-gfp*	1% xylose	this work
B. subtilis HS39	*tet amyE::Pxyl-fruA-gfp*	1% xylose	this work
B. subtilis HS40	*tet amyE::Pxyl-p16.7-gfp*	1% xylose	this work
B. subtilis HS41	*tet amyE::Pxyl-yhaP-gfp*	1% xylose	this work
B. subtilis HS42	*tet amyE::Pxyl-yqfD-gfp*	1% xylose	this work
B. subtilis HS43	*tet amyE::Pxyl-rny-gfp*	1% xylose	this work
	Ωneo3427ΔmreB Δmbl::cat		
	ΔmreBH::erm ΔrsgI::spc		
B. subtilis HS44	*tet amyE::Pxyl-fruA-gfp*	1% xylose	this work
	Ωneo3427ΔmreB Δmbl::cat		
	ΔmreBH::erm ΔrsgI::spc		
B. subtilis HS45	*tet amyE::Pxyl-p16.7-gfp*	1% xylose	this work
	Ωneo3427ΔmreB Δmbl::cat		
	ΔmreBH::erm ΔrsgI::spc		
B. subtilis HS46	*tet amyE::Pxyl-yhaP-gfp*	1% xylose	this work
	Ωneo3427ΔmreB Δmbl::cat		
	ΔmreBH::erm ΔrsgI::spc		
B. subtilis HS47	*tet amyE::Pxyl-yqfD-gfp*	1% xylose	this work
	Ωneo3427ΔmreB Δmbl::cat		
	ΔmreBH::erm ΔrsgI::spc		
C. glutamicum RES167		-	20
S. aureaus RN4220		-	21

Supplementary Table 3: Oligonucleotides

Oligonucleotide	Sequence
mreD-for	GCGCGAAGCTTTAACAGATGACCAAGTGCTCGCC
mreD-rev 1-172	GCGCGGGATCCTTACTCATCTCTCAATTCTTTCTTTAG
mreD-rev 1-157	GCGCGGGTACCTTATGGCAGAACAAGAATAAGAGC
GFPA206K-for	CCTGTCCACACAATCTAAACTTTCGAAAGATCCC
GFPA206K-rev	GGGATCTTTCGAAAGTTTAGATTGTGTGGACAGG
pSG1154-for	GCTAATTTTATTGCAATAACAGGTG
pSG1154-rev	GACCGTTAGCGTTTAAGTACATC
tetR-for	TGCAATAAAATTAGCCTGCAGGTCGATATGAACAGC
tetR-rev	TAAACGCTAACGGTCCTCTCTCCCAAAGTTGATCC
pSG1154-for2	GAACTATACAAATAAATGTCCAGAC
pSG1154-rev2	CCGACAGGCTTTGAAGCATG
Pxyl-for	TTCAAAGCCTGTCGGAATTGG
GFP-rev	TTATTTGTATAGTTCATCCATGCC

SUPPLEMENTARY METHODS

Bacterial strains and growth conditions

The used strains, and conditions for gene induction are listed in Table S2. All *B. subtilis* strains were grown in the absence of antibiotics in LB medium at 30 °C, if not stated otherwise. LB supplemented with 20 mM MgCl$_2$ was used to grow the *mreB, mbl, mreBH, mreC* and *mreD* deletion strains. The MreD-truncation mutant exhibits MreB delocalization under low Mg^{2+} concentration conditions. The effect was most apparent when cells were transferred from high Mg^{2+} medium (PAB + 20 mM MgCl$_2$) to low Mg^{2+} medium (PAB). Microscopy was carried out after 60 min incubation in low Mg^{2+} medium. To test the effect of valinomycin or nigericin, *B. subtilis* cells were grown in yeast extract-peptone medium supplemented with 50 mM Hepes-HCl pH 7.5, and 300 mM KCl.

ΔΨ of *B. subtilis* was dissipated by the addition of 30 μM valinomycin, and the ΔpH by addition of 5 μM nigericin directly to the culture medium[1], followed by 2 min incubation. Dissipation of the pmf in the different bacteria was established by the addition of 100 μM CCCP in all bacteria tested, as described before [1, 22, 23]. For inhibition of the dynamic movement of the cytoskeleton [24]., *B. subtilis* cells were incubated for 3 min with 2 μg/ml

vancomycin. For localization of Lipid II, cells were incubated for 5 min with 0.5 μg/ml fluorescein-labelled vancomycin (Van-FL) mixed with an equal concentration of unlabelled vancomycin [8].

Construction of strains

The strain encoding a truncation of *mreD* was constructed by amplification of an internal *mreD*-fragment using the oligonucleotides mreD-for, and mreD-rev1-157 (see Table S3), followed by cloning into pMutin4 [25] using restriction sites *Hin*dIII and *Bam*HI. Finally, the plasmid was integrated into *B. subtilis* 168 resulting in strain HS32 that encodes a C-terminal 15 amino acid truncation of MreD. Strain HS31 was constructed as a control to rule out possible polar effects of the pMutin4 integration. In this case, the intact (non-truncated) 3'-end of *mreD* was amplified using oligonucleotides mreD-for and mreD-rev1-172, followed by cloning and integration into *B. subtilis* 168. As a result, this strain does not carry a truncation of MreD but contains an integrated pMutin4 plasmid in the same locus.

The strain *B. subtilis* HS37 encoding GFP-MreB with a GFP$_{A206K}$ exchange to prevent dimerization of GFP, was constructed by quick change method using primers GFPA206K-for and GFPA206K-rev followed and integration into the *amyE* locus of *B. subtilis* 168.

In order to analyse the CCCP-dependent localization of membrane proteins in the absence of MreB-homologs, an exchange of resistance markers was necessary. For this, the *amyE*-integration plasmid pSG1154 [26] was PCR-linearized using oligos pSG1154-for/pSG1154-rev, and tetR amplified from pBEST309 [27] using oligos tetR-for/tetR-rev. The PCR products were fused using In-Fusion HD Plus restriction free cloning kit (Clontech) resulting in pSG1154tetR. The protein-GFP fusions were amplified from chromosomal DNA of the corresponding *B. subtilis* strains using oligos Pxyl-for/GFP-rev, and integrated into pSG1154tetR PCR-linearized with oligos pSG1154-for2/pSG1154-rev2 using In-Fusion

cloning. The resulting plasmids were sequenced, and integrated into *B. subtilis* genome resulting in strains HS38-HS42. At last, the *mreB*-homologs were successively deleted in the order Δ*rsgI::spc*, Δ*mreBH::erm*, Δ*mbl::cat* and Ω*neo3427* Δ*mreB* resulting in strains HS43-47.

SUPPLEMENTARY REFERENCES

1. Strahl H, Hamoen LW. Membrane potential is important for bacterial cell division. *Proc Natl Acad Sci U S A* **107**, 12281-12286 (2010).

2. Wasungu L, Stuart MCA, Scarzello M, Engberts JBFN, Hoekstra D. Lipoplexes formed from sugar-based gemini surfactants undergo a lamellar-to-micellar phase transition at acidic pH. Evidence for a non-inverted membrane-destabilizing hexagonal phase of lipoplexes. *Biochim Biophys Acta* **1758**, 1677-1684 (2006).

3. Silva JPN, Oliveira MECDR, Coutinho PJG. Characterization of mixed DODAB/monoolein aggregates using Nile Red as a solvatochromic and anisotropy fluorescent probe. *J Photoch Photobio A* **203**, 32-39 (2009).

4. G Greenspan P, Fowler SD. Spectrofluorometric studies of the lipid probe, nile red. *J Lipid Res* **26**, 781-789 (1985).

5. Barak I, Muchova K, Wilkinson AJ, O'Toole PJ, Pavlendova N. Lipid spirals in *Bacillus subtilis* and their role in cell division. *Mol Microbiol* **68**, 1315-1327 (2008).

6. Muchova K, Wilkinson AJ, Barak I. Changes of lipid domains in *Bacillus subtilis* cells with disrupted cell wall peptidoglycan. *Fems Microbiol Lett* **325**, 92-98 (2011).

7. Li Q, Lau A, Morris TJ, Guo L, Fordyce CB, Stanley EF. A syntaxin 1, G alpha(o), and N-type calcium channel complex at a presynaptic nerve terminal: Analysis by quantitative immunocolocalization. *J Neurosci* **24**, 4070-4081 (2004).

8. Daniel RA, Errington J. Control of cell morphogenesis in bacteria: Two distinct ways to make a rod-shaped cell. *Cell* **113**, 767-776 (2003).

9. Barbe V, *et al.* From a consortium sequence to a unified sequence: the *Bacillus subtilis* 168 reference genome a decade later. *Microbiology* **155**, 1758-1775 (2009).

10. Formstone A, Errington J. A magnesium-dependent *mreB* null mutant: implications for the role of *mreB* in *Bacillus subtilis*. *Mol Microbiol* **55**, 1646-1657 (2005).

11. Schirner K, Errington J. The cell wall regulator σI specifically suppresses the lethal phenotype of *mbl* mutants in *Bacillus subtilis*. *J Bacteriol* **191**, 1404-1413 (2009).

12. Kawai Y, Daniel RA, Errington J. Regulation of cell wall morphogenesis in *Bacillus subtilis* by recruitment of PBP1 to the MreB helix. *Mol Microbiol* **71**, 1131-1144 (2009).

13. Johnson AS, van Horck S, Lewis PJ. Dynamic localization of membrane proteins in *Bacillus subtilis*. *Microbiology* **150**, 2815-2824 (2004).

14. Meijer WJ, Serna-Rico A, Salas M. Characterization of the bacteriophage phi29-encoded protein p16.7: a membrane protein involved in phage DNA replication. *Mol Microbiol* **39**, 731-746 (2001).

15. Meile JC, Wu LJ, Ehrlich SD, Errington J, Noirot P. Systematic localisation of proteins fused to the green fluorescent protein in *Bacillus subtilis*: Identification of new proteins at the DNA replication factory. *Proteomics* **6**, 2135-2146 (2006).

16. Hunt A, Rawlins JP, Thomaides HB, Errington J. Functional analysis of 11 putative essential genes in *Bacillus subtilis*. *Microbiology* **152**, 2895-2907 (2006).

17. Salzberg LI, Helmann JD. Phenotypic and transcriptomic characterization of *Bacillus subtilis* mutants with grossly altered membrane composition. *J Bacteriol* **190**, 7797-7807 (2008).

18. Hachmann AB, Angert ER, Helmann JD. Genetic analysis of factors affecting susceptibility of *Bacillus subtilis* to daptomycin. *Antimicrob Agents Chemother* **53**, 1598-1609 (2009).

19. Kobayashi K, *et al.* Essential *Bacillus subtilis* genes. *Proc Natl Acad Sci U S A* **100**, 4678-4683 (2003).

20. Tauch A, Kirchner O, Loffler B, Gotker S, Puhler A, Kalinowski J. Efficient electrotransformation of *Corynebacterium diphtheriae* with a mini-replicon derived from the *Corynebacterium glutamicum* plasmid pGA1. *Curr Microbiol* **45**, 362-367 (2002).

21. Kreiswirth BN*, et al.* The toxic shock syndrome exotoxin structural gene is not detectably transmitted by a prophage. *Nature* **305**, 709-712 (1983).

22. Bayan N, Schrempp S, Joliff G, Leblon G, Shechter E. Role of the protonmotive force and of the state of the lipids in the *in vivo* protein secretion in *Corynebacterium glutamicum*, a gram-positive bacterium. *Biochim Biophys Acta* **1146**, 97-105 (1993).

23. Patton TG, Yang SJ, Bayles KW. The role of proton motive force in expression of the *Staphylococcus aureus cid* and *lrg* operons. *Mol Microbiol* **59**, 1395-1404 (2006).

24. Garner EC, Bernard R, Wang W, Zhuang X, Rudner DZ, Mitchison T. Coupled, circumferential motions of the cell wall synthesis machinery and MreB filaments in *B. subtilis*. *Science* **333**, 222-225 (2011).

25. Vagner V, Dervyn E, Ehrlich SD. A vector for systematic gene inactivation in *Bacillus subtilis*. *Microbiology* **144 (Pt 11)**, 3097-3104 (1998).

26. Lewis PJ, Marston AL. GFP vectors for controlled expression and dual labelling of protein fusions in *Bacillus subtilis*. *Gene* **227**, 101-110 (1999).

27. Itaya M. Construction of a novel tetracycline resistance gene cassette useful as a marker on the *Bacillus subtili*s chromosome. *Biosci Biotech Bioch* **56**, 685-686 (1992).